*energies*

MDPI

*Article*

# An Energy-Efficient Control Allocation Strategy for PTC Heater-Based Electric Vehicle Cabin Thermal Management

**Luka Grden [1], Branimir Škugor [1], Joško Deur [1,*] and Ivan Cvok [2]**

[1] University of Zagreb, Faculty of Mechanical Engineering and Naval Architecture, 10002 Zagreb, Croatia; luka.grden@fsb.unizg.hr (L.G.); branimir.skugor@fsb.unizg.hr (B.Š.)
[2] Rimac Technology d.o.o., Kerestinec, 10431 Sveta Nedelja, Croatia; ivan.cvok@rimac-technology.com
* Correspondence: josko.deur@fsb.unizg.hr

**Abstract**

Electric vehicles (EVs) experience substantially reduced driving range in cold weather, primarily due to cabin heating energy demands. This paper proposes a control allocation strategy for positive temperature coefficient (PTC) heater-based electric minibus cabin thermal management, aimed at minimizing energy consumption. The strategy is of a hierarchical structure, where a supervisory PI cabin temperature controller commands the heating power demand, which is then achieved through optimal allocation and low-level control of the cabin inlet air temperature, coolant pump flow, and radiator blower air flow control inputs. Based on the assumption of fast heating system dynamics relative to cabin thermal dynamics, quasi-steady-state optimization of control input allocation is carried out by employing a grid-search algorithm over a dataset resulting from high-fidelity simulations. For the system heat-up transient conditions, where the steady-state allocation proves to be suboptimal, dynamic programming is applied on a validated reduced-order model to optimize the control trajectories. Insights gained through control trajectory optimization are then used to develop a rule-based modification of the control allocation strategy for the heat-up scenario. Simulation verification of the overall control system demonstrates energy consumption reduction in the range from 4 to 12% when compared to the industrial baseline system across both steady-state and transient operating conditions.

**Keywords:** electric vehicle; PTC heater; energy efficiency; optimization; control allocation; dynamic programming; rule-based control

## 1. Introduction

Driving range reduction at extreme ambient temperatures remains one of the principal drawbacks of electric vehicles (EVs) [1]. This is because of increased battery electricity consumption by the vehicle heating, ventilation and air-conditioning (HVAC) system. In [2] it is reported that typical electric vehicle heating systems may consume from 6 to 9 kW of electric power in harsh winter conditions, which can reduce the driving range by approximately 30 to 50%. EV cabin heating is conventionally provided by a high-voltage positive temperature coefficient (PTC) heater, as a cost-effective and robust solution [3]. In addition to the PTC heater itself, these systems employ auxiliary actuators such as cabin blower fans and coolant pumps. The primary limitation of PTC heaters is that their coefficient of performance (COP) cannot exceed 1, i.e., the heating energy is equal to the consumed electric energy. To overcome this weakness, heat-pump systems have recently been introduced in EV cabin HVAC systems, which can achieve significantly higher COP

Check for updates

Academic Editor: Rui Xiong

Received: 10 February 2026
Revised: 7 March 2026
Accepted: 13 March 2026
Published: 24 March 2026

**Copyright:** © 2026 by the authors. Licensee MDPI, Basel, Switzerland. This article is an open access article distributed under the terms and conditions of the Creative Commons Attribution (CC BY) license.

values through exploiting the ambient heat, as well as the powertrain and battery waste heat [4]. However, these systems exhibit nonlinear, coupled thermal dynamics with actuator redundancy, which poses challenges for thermal management [5]. To operate efficiently, such multi-actuator PTC heater and heat-pump systems require advanced control strategies capable of coordinating multiple control actions in an optimal manner [6].

A range of HVAC control approaches have been reported in the literature. A rule-based proportional–integral–derivative (PID) controller is applied in [7] to the conventional HVAC system to manipulate the blower air flow in dependence on the calculated thermal load. The controller gains are scheduled by a neural network with respect to ambient conditions. PID control is also considered in [3], where an additional feedforward action is employed to mitigate the effect of system lag, which is commonly observed in coolant-to-air heating systems. Robust EV thermal management based on H-infinity control has been investigated for EV thermal management in [8], offering guaranteed stability and disturbance attenuation in the presence of modeling uncertainties. Here the controller feedback gains are derived through an iterative process of HVAC model linearization and solving the Riccati equation. Since the HVAC system control-oriented physical modeling can pose a certain challenge related to loss of accuracy when compared to original high-fidelity models [9], data-driven control techniques are also employed, including reinforcement learning-based approaches [10].

To minimize the power/energy consumption while maintaining favorable thermal comfort, HVAC control strategies are increasingly relying on optimization-based control methods [11]. An advanced hierarchical control strategy is proposed in [12] to coordinate multiple actuators of a heat-pump system. Here, an optimal allocation of actuator inputs is executed with respect to heating power demand and cabin temperature, where the allocation maps are obtained via multi-objective genetic algorithm (GA)-based offline optimization [13]. Apart from instantaneous optimization, control trajectory optimization techniques are also considered [14]. For a broad group of nonlinear, time-variant systems with nonlinear constraints, which the HVAC systems belong to, a globally optimal solution can be derived by using the dynamic programming (DP) algorithm [15]. Since DP is computationally expensive, a prerequisite for its application is that the system size (i.e., the number of state and control variables) is relatively small. In [16], stochastic dynamic programming is applied to optimize the operation of an electric bus air-conditioning system by accounting for time-varying uncertainty in passenger-induced thermal loads.

Globally optimal solutions are often used for system analysis and serve as a basis for real-time control strategy development [17], as well as a performance benchmark [18]. In [19] DP is applied to optimize air-conditioning compressor clutch control trajectories, based on which a control policy is derived using the Pontryagin minimum principle. Similarly, insights obtained through globally optimal offline control trajectory optimization are employed in [20] to extend the control allocation strategy towards improving its transient performance. In addition to offline optimization-inspired approaches, online control trajectory optimization techniques are also used, typically through a model predictive control (MPC) framework [21], offering improved performance and thermal comfort in both transient and quasi-stationary conditions [22], as well as control system design flexibility [23]. In [24], the HVAC control strategy is extended toward an integrated thermal management approach, including battery thermal conditioning. A nonlinear MPC framework is set up to optimally and predictively coordinate different subsystems, demonstrating considerable improvements in energy efficiency under cold ambient conditions. A fuel-cell electric bus energy management strategy is proposed in [25], based on reinforcement learning, where passenger occupancy estimation is utilized to accurately observe the corresponding cabin thermal load and overall vehicle energy demand. An alternative approach to passenger

cabin heating is explored in [26], where ceiling-mounted radiant heating panels are investigated as a supplemental option to conventional PTC- and heat-pump-based HVAC systems. The optimal coordination of the PTC heater and radiant heating panels demonstrates a reduction in HVAC power consumption compared with PTC-only heating of up to 7% [27].

Although the benefits of applying the heat-pump systems in EVs are clearly recognized [28], PTC heating systems continue to be applied for cost efficiency reasons. Also, the efficiency of heat pumps can be sensitive to ambient disturbances and deteriorates under very cold climate conditions, so they are usually combined with a supplementary PTC heater anyway [29,30]. Moreover, as shown in [31], such hybrid architectures can operate more efficiently because of keeping the heat-pump compressor closer to its optimal operating region.

In summary, EV thermal management systems are becoming increasingly complex due to the growing number of interacting subsystems and operating constraints. Advanced control strategies such as MPC- and RL-based approaches have been investigated to improve energy efficiency and system coordination in an optimal and predictive manner. However, these approaches typically require high computational power or extensive training, and can be sensitive to modeling/training errors, which hinders their implementation and certification in production vehicle controllers. To address these challenges, this paper extends and consolidates the control allocation framework, previously introduced for a heat-pump HVAC system in [12,20], towards achieving near-optimal performance while maintaining a computationally efficient and interpretable control structure. While the earlier contributions inherently narrow the optimal control allocation to (quasi-) stationary conditions, this article advances the methodology towards a PTC heater-based HVAC architecture and explicitly addresses transient operation through an additive dynamic-optimization-inspired, rule-based allocation strategy. The core of the strategy relates to optimal allocation maps for the cabin inlet air temperature, cabin blower air mass flow, and pump flow control inputs. The control allocation maps are derived through offline optimization for a grid of heating power demand and cabin temperature operating points. The heating power demand is determined by a parameter-optimized superimposed proportional–integral (PI) controller. An analytically optimized low-level PI controller of allocated cabin inlet air temperature outputs the PTC heater power. The overall control system is verified through computer simulations involving a high-fidelity thermal system model, and the results are compared to those obtained through simulating an industry baseline system mimicking the on-vehicle control strategy.

The main contributions of the paper can be summarized as: (i) control allocation for a PTC heater-based system providing minimal energy consumption for steady-state conditions, (ii) control trajectory optimization for a heat-up transient scenario involving a validated reduced-order HVAC model and a globally optimal dynamic programming (DP) algorithm, and (iii) a DP optimization-inspired additive rule-based control strategy evaluated against the DP benchmark. Although the paper is focused on PTC heater-based HVAC systems, the proposed optimization and optimal control methods are applicable to heat-pump and A/C systems as well.

The remainder of this paper is organized as follows. Section 2 outlines the high-fidelity HVAC and cabin system model, as well as the corresponding reduced-order model utilized in control trajectory optimization. Section 3 presents the control trajectory optimization approach and related results. Section 4 presents the overall hierarchical control framework, including the control allocation strategy, and the rule-based and low-level controllers. Section 5 presents the superimposed cabin temperature controller design. Section 6 elaborates on verification of the basic hierarchical control allocation strategy against the industry baseline for both stationary and heat-up conditions. Section 7 extends upon the verification

of the control allocation strategy supplemented with the rule-based controller against the control trajectory optimization benchmark and the basic control allocation strategy for heat-up conditions. Concluding remarks are given in Section 8.

## 2. HVAC and Cabin System Model

The models presented in this section serve as a foundation for control strategy development, optimization, and simulation verification. They include a high-fidelity distributed-parameter model and a substantially simplified reduced-order nonlinear model.

### *2.1. High-Fidelity Model*

#### 2.1.1. HVAC Model

The electric minibus cabin heating system comprises the driver and passenger subsystems, each of which is based on a PTC heater. The driver cabin heating subsystem is controlled independently in automatic mode, and it is modeled separately together with its controller and a proper heat exchange path towards the passenger cabin. The passenger cabin subsystem is the subject of the optimal control strategy developed in this paper. It should be noted that, apart from the PTC heater, the passenger cabin HVAC system includes (i) an additional fuel-powered heating system used for extremely cold ambient conditions and/or low battery state-of-charge (SoC), and (ii) a separate A/C system employed for cabin cooling [32]. These separate systems are not considered in this paper, as it is focused on heating through the main, fully controllable, and ecological control channel relying on the PTC heater. The proposed control strategy would apply in the case of supplemental fuel heating as well, but it may be subject to gain scheduling depending on the supplemental heating power, which is a practical aspect that falls beyond the scope of the paper. For the sake of brevity, the considered passenger cabin heating system is further referred to as the HVAC system.

The HVAC system behavior is represented by a high-fidelity, multi-physics simulation model implemented in the Dymola environment (Figure 1), which has been experimentally validated against measurement data from [32]. The validation was performed for cold ambient conditions (the ambient temperature and the initial cabin temperature were set to 0 °C as in this study, as well as to −7 °C in an additional validation run), the vehicle velocity followed the WLTP driving cycle adjusted to account for the electric minibus maximum velocity limit, no passenger occupancy, full air recirculation, full passenger cabin heating system power, the driver cabin heating temperature reference set to 23 °C, and the heating-up period of 9300 s (corresponding to the five consecutive adapted WLTP driving cycles), which resulted in a final cabin temperature of 18 °C [33]. The model was found to reproduce the corresponding measured cabin temperatures (sampled in 12 different points across three different minibus seats) with an error margin of ±1.6 °C, while the discrepancy in model-predicted electric power consumption was below 8% [32]. The system includes three actuators: a PTC heater, water–glycol coolant pump, and air blower fan associated with a coolant-to-air heat exchanger (radiator) situated in the upper-left part of the cabin. The corresponding control inputs are the PTC heater power setpoint $P_{PTC}$, the volumetric coolant pump flow $\dot{V}_p$, and the volumetric blower fan air flow $\dot{V}_{bf}$. The relevant HVAC model outputs include the cabin heating core outlet/cabin inlet temperature $T_{in}$, the PTC heater outlet coolant temperature $T_{clnt}$, the blower fan air mass flow rate $\dot{m}_{bf}$, and the corresponding actuator power consumptions $P_{PTC}$, $P_p$, and $P_{bf}$. The power consumptions of the air blower fan and the coolant pump are approximated by 1D maps shown in Figure 2, and fed by the corresponding control input.

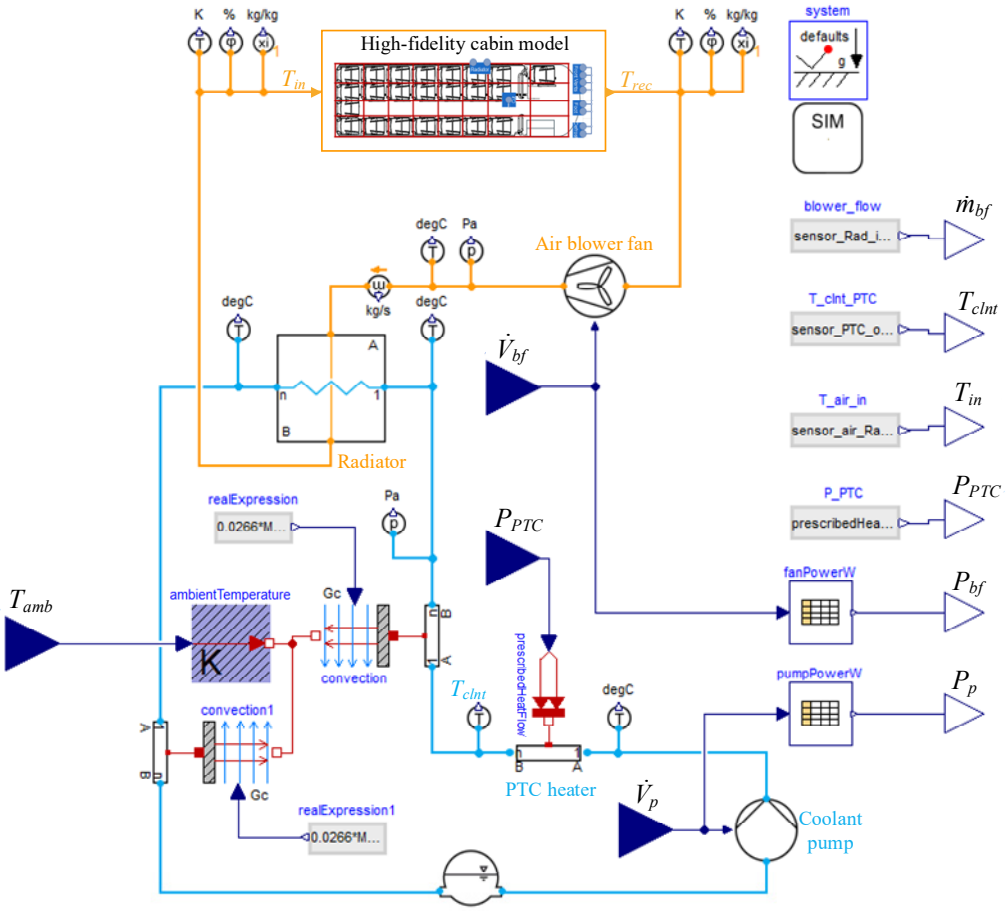



**Figure 1.** Passenger cabin heating system model implemented in Dymola environment.

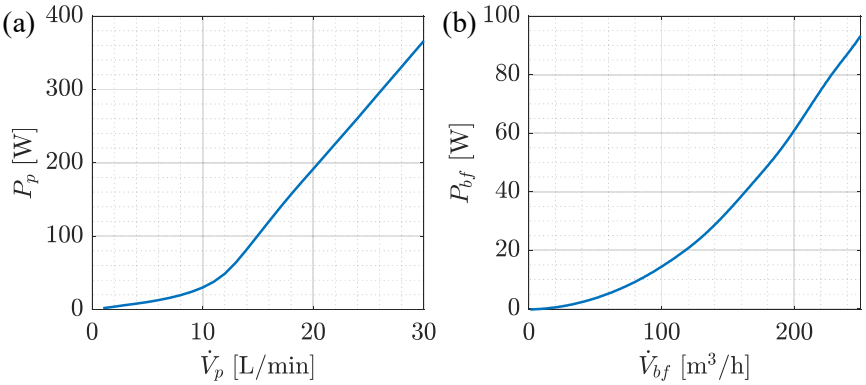



**Figure 2.** Power consumption maps for coolant pump (**a**) and blower fan (**b**).

### 2.1.2. Cabin Model

The cabin is represented by a multi-zonal control-volume moist air model consisting of 45 volumes (Figure 3), which captures non-uniform air temperature distribution in the horizontal and vertical directions. The model has been developed by using the XRG Dymola Library and parameterized based on available data related to measurements conducted at three distinct seats for the external/ambient temperature $T_{amb}$ = 0 °C (see [32] for more details). The air temperature in the middle of the passenger cabin aisle ($T_{cab}$ in Figure 3) is chosen as a representative cabin temperature used in the control strategy design and evaluation.

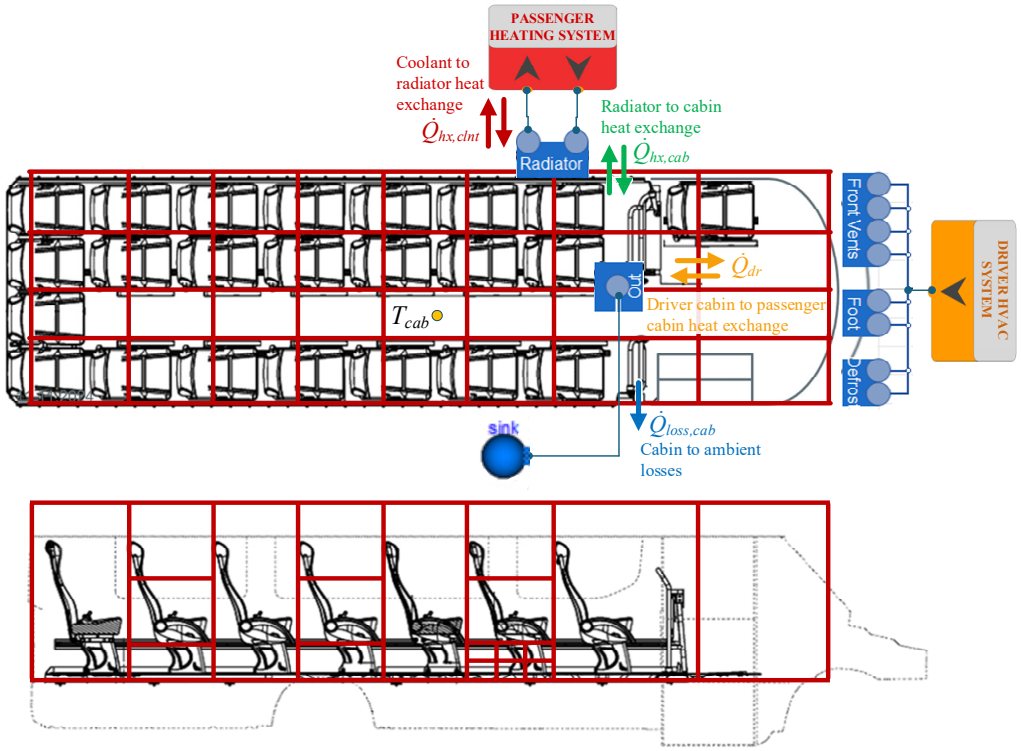



**Figure 3.** Illustration of multi-zonal control-volume passenger cabin model.

### *2.2. Reduced-Order Model*

The reduced-order model aims to capture the dominant thermal dynamics characterized by only two lumped thermal masses: (i) the coolant with the thermal capacity $C_{clnt}$ and the temperature $T_{clnt}$, and the cabin air and body with the thermal capacity $C_{cab}$ and the temperature $T_{cab}$. The corresponding state equations read as follows:

$$C_{clnt}\dot{T}_{clnt} = P_{PTC} - \dot{Q}_{hx,clnt} - \dot{Q}_{loss,clnt}, \quad (1)$$

$$C_{cab}\dot{T}_{cab} = \dot{Q}_{hx,cab} + \dot{Q}_{dr} - \dot{Q}_{loss,cab}. \quad (2)$$

The coolant is heated by the PTC heater via the corresponding power control input $P_{PTC}$. The heating power $\dot{Q}_{hx,clnt}$ is transferred through the coolant-to-air heat exchanger (radiator) to be delivered to the passenger cabin:

$$\dot{Q}_{hx,clnt} = \dot{V}_p \rho_{clnt} c_{clnt} (T_{clnt} - T_{clnt,out}), \quad (3)$$

where $\dot{V}_p$ is the coolant (pump) flow control input, $\rho_{clnt}$ is the coolant density, $c_{clnt}$ is the coolant specific heat capacity, and $T_{clnt} - T_{clnt,out}$ is the difference in coolant temperature on the inlet and outlet of the radiator. The coolant experiences heat losses along the piping, which are modeled through the following quadratic relation (adopted from the high-fidelity model [32]):

$$\dot{Q}_{loss,clnt} = a_{c1}(T_{clnt} - T_{amb})^2, \quad (4)$$

where $a_{c1}$ is the corresponding heat transfer-related parameter, and $T_{amb}$ is the ambient temperature. On the other hand, the cabin thermal mass from Equation (2) is heated by the driver-side HVAC subsystem thermal load $\dot{Q}_{dr}$ (modeled here as a tuned constant), and primarily by the radiator air-side heat transfer:

$$\dot{Q}_{hx,cab} = \dot{V}_{bf} \rho_{cab} c_{p,cab} (T_{in} - T_{cab}), \quad (5)$$

where $\dot{V}_{bf}$ is the blower fan air flow control input, $\rho_{cab}$ is the air density, $c_{p,cab}$ is the specific heat capacity at constant air pressure, and $T_{in} - T_{cab}$ is the difference between the cabin inlet air temperature and the air temperature in the cabin. The cabin thermal losses to the ambient are modeled as

$$\dot{Q}_{loss,cab} = a_{c2}(T_{cab} - T_{amb}), \tag{6}$$

where $a_{c2}$ is the cabin-to-ambient heat transfer-related parameter.

To retain the second-order model form given by Equations (1) and (2), i.e., to omit the fast radiator heat exchange dynamics, the coolant- and air-side heat transfers of the radiator are equalized:

$$\dot{Q}_{hx,clnt} = \dot{Q}_{hx,cab}. \tag{7}$$

Neglecting the radiator dynamics is justified by the observation that, based on the high-fidelity model response, the cabin inlet temperature follows the coolant temperature with a minor delay. Based on Equations (3), (5) and (7) one can express the cabin inlet temperature through a static model:

$$T_{in} = f_{T_{in}}\left(T_{clnt}, T_{cab}, \dot{V}_{bf}, \dot{V}_p\right). \tag{8}$$

Note that the variable $T_{clnt,out}$ from Equation (3) can also be described as a function of the same arguments given in Equation (8), so that it is effectively included in the model (8).

To describe the nonlinear static function $f_{T_{in}}(.)$ in Equation (8), a polynomial regression model is fitted to the dataset derived from an extensive set of high-fidelity model transient simulations executed for different model inputs $T_{clnt}$, $T_{cab}$, $\dot{V}_{bf}$, and $\dot{V}_p$ (see Section 4 for a description of the simulations). A quadratic model with interaction terms is selected through a feature selection method and identified by the least-squares method. For this purpose, the MATLAB R2025b *stepwiselm(.)* function and the Akaike information criterion [34] are used. The selected model reads

$$\begin{aligned} T_{in} = {} & b_{T_{in}0} + b_{T_{in}1}T_{clnt} + b_{T_{in}2}\dot{V}_{bf} + b_{T_{in}3}\dot{V}_p + b_{T_{in}4}T_{cab} + b_{T_{in}5}T_{clnt}\dot{V}_{bf} \\ & + b_{T_{in}6}T_{clnt}\dot{V}_p + b_{T_{in}7}T_{clnt}T_{cab} + b_{T_{in}8}\dot{V}_{bf}\dot{V}_p + b_{T_{in}9}\dot{V}_{bf}T_{cab} \\ & + b_{T_{in}10}\dot{V}_pT_{cab} + b_{T_{in}11}\dot{V}_p^2. \end{aligned} \tag{9}$$

Figure 4 shows the model validation results obtained on a separate dataset. They indicate high modeling accuracy, characterized by the root mean square error (RMSE) of 0.92 °C for the full-scale output of around 90 °C and a nearly ideal coefficient of determination $R^2 = 0.98 \cong 1$.

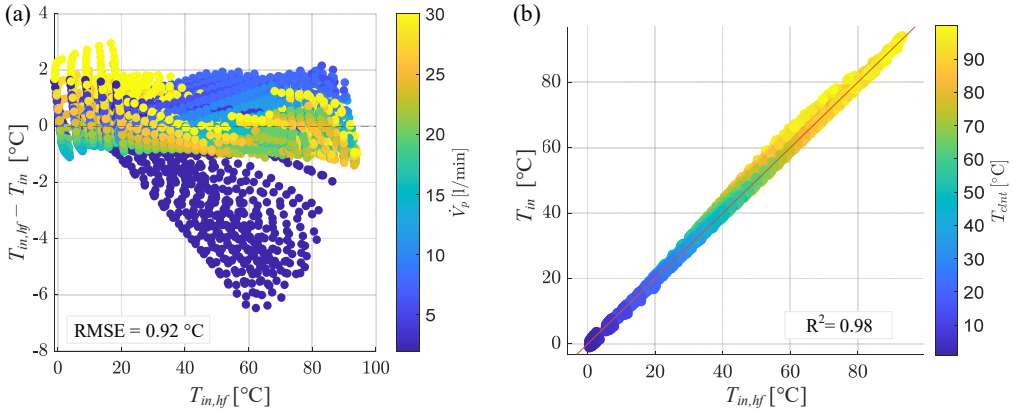



**Figure 4.** Results of cabin inlet temperature quadratic model assessment: model residuals (**a**) and modeled vs. actual inlet temperature (**b**), including corresponding RMSE and $R^2$ metrics (actual inlet temperature $T_{in,hf}$ is taken from high-fidelity model).

Combining Equations (1)–(3), (5), (7) and (8), one obtains the final reduced-order model:

$$C_{clnt}\dot{T}_{clnt} = P_{PTC} - \dot{V}_{bf}\rho_{cab}c_{p,cab}\left(f_{T_{in}}\left(T_{clnt}, T_{cab}, \dot{V}_{bf}, \dot{V}_p\right) - T_{cab}\right) - a_{c1}(T_{clnt} - T_{amb})^2, \quad (10)$$

$$C_{cab}\dot{T}_{cab} = \dot{Q}_{dr} + \dot{V}_{bf}\rho_{cab}c_{p,cab}\left(f_{T_{in}}\left(T_{clnt}, T_{cab}, \dot{V}_{bf}, \dot{V}_p\right) - T_{cab}\right) - a_{c2}(T_{cab} - T_{amb}), \quad (11)$$

whose parameters are contained in the vector

$$\mathbf{p} = \left[C_{clnt}C_{cab} \;\; a_{c1}a_{c2} \;\; \dot{Q}_{dr}\right], \quad (12)$$

and identified by solving the nonlinear least-squares problem using the MATLAB *fmincon(.)* function:

$$\mathbf{p}^* = \underset{\mathbf{p}}{\operatorname{argmin}} \sum_{k=1}^{N_t} \left\| \mathbf{y}(k, \mathbf{p}) - \mathbf{y}_{hf}(k) \right\|^2, \quad (13)$$

where $\boldsymbol{y}\,(k, \mathbf{p}) = [T_{clnt} \;\; T_{cab}]^{\mathrm{T}}$ denotes the response of the discrete-time version of the above reduced-order model, obtained by applying the forward Euler integrator approximation with the sampling time $\tau_s = 5$ s, while $\mathbf{y}_{hf}$ represents the high-fidelity model outputs sampled with the same sampling time for the transient scenarios described in Section 6.

The identified reduced-order model is validated against an independent high-fidelity model response for the heat-up regime and the initial cabin temperature equal to the ambient temperature of 0 °C. The excitation signals $P_{PTC}$, $\dot{V}_{bf}$ and $\dot{V}_p$ applied to both models correspond to those obtained by applying the control allocation strategy designed in Section 4 to the high-fidelity model. The comparative verification results are shown in Figure 5. The reduced-order vs. high-fidelity model residuals concerning the coolant temperature, cabin temperature, and inlet temperature transient responses extracted in the zoom-in plot of Figure 5 constitute $R^2$ indices of 0.96, 0.63 and 0.97, respectively, while the corresponding RMSEs are 2.0, 3.8 and 2.6 °C, respectively. This may be considered solid modeling accuracy, bearing in mind the substantial model order reduction made. The relatively low cabin temperature fitting accuracy ($R^2$ = 0.63) may be expected, because the high-fidelity cabin model includes multi-zonal and non-uniform heat transfer effects, which cannot be faithfully captured by the lumped, single-zone low-order model (11).

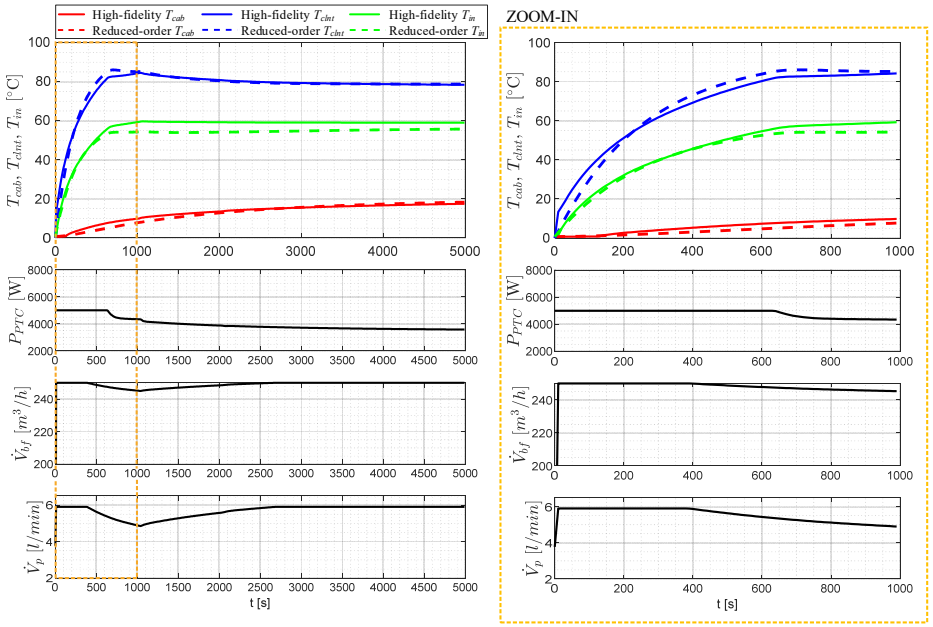



**Figure 5.** Reduced-order model validation results for heat-up scenario.

## 3. Control Trajectory Optimization

A control trajectory optimization algorithm is developed in this section, in order to gain insight into globally optimal HVAC system behavior under the heat-up conditions.

### *3.1. Optimization Problem Formulation*

The offline control trajectory optimization is based on the dynamic programming (DP) algorithm, which decomposes a complex optimization problem into simpler recursive subproblems [15]. DP solves each subproblem backward in time starting from a final condition and stores its optimal solutions in its memory. It then uses the stored solutions to reconstruct the optimal trajectory forward in time starting from the specified initial conditions. DP is characterized by its unique feature of guaranteeing the global optimality of a solution for general optimization problems with a non-convex cost function and constraints.

The optimization objective is to minimize the total HVAC energy consumption over the defined heat-up time horizon while ensuring that the prescribed cabin temperature is reached at the terminal time step and that all operational constraints are satisfied. The total HVAC energy consumption to be minimized is defined as

$$J_0 = \sum_{k=0}^{N_f-1} P_{HVAC}(k)\tau_s \tag{14}$$

where $k$ is the discrete-time step corresponding to the interval $t_k = k\tau_s$, $k = 0, 1, \ldots, N_f - 1$, with $\tau_s$ denoting the sampling time. The term $P_{HVAC}(k)$ is the HVAC system power consumption, determined as

$$P_{HVAC}(k) = P_{PTC}(k) + P_p\left(\dot{V}_p(k)\right) + P_{bf}\left(\dot{V}_{bf}(k)\right), \tag{15}$$

where $P_{PTC}(k)$, $\dot{V}_p(k)$, and $\dot{V}_{bf}(k)$ represent the control variables to be optimized while $P_p\left(\dot{V}_p(k)\right)$ and $P_{bf}\left(\dot{V}_{bf}(k)\right)$ are the 2D power consumption curves shown in Figure 2.

The problem is subject to the discrete-time version of the reduced-order process state-space model given by Equations (10) and (11). The final condition is defined as

$$T_{cab}(N_f) = T_{cab,f}, \tag{16}$$

requiring that the cabin temperature at the end is at the prescribed value $T_{cab,f}$. The following lower and upper constraints are imposed on the state, control, and output variables:

$$0 \le T_{cab}\ [^\circ\mathrm{C}] \le T_{cab,\max}, \tag{17a}$$

$$0 \le T_{clnt}\ [^\circ\mathrm{C}] \le T_{clnt,\max}, \tag{17b}$$

$$\dot{V}_{p,\min} \le \dot{V}_p\ [\mathrm{L/min}] \le \dot{V}_{p,\max}, \tag{17c}$$

$$\dot{V}_{bf,\min} \le \dot{V}_{bf}\ \left[\mathrm{m^3/h}\right] \le \dot{V}_{bf,\max}, \tag{17d}$$

$$0 \le P_{PTC}\ [\mathrm{W}] \le P_{PTC,\max}. \tag{17e}$$

$$T_{in}\ [^\circ\mathrm{C}] \le T_{in,\max}, \tag{17f}$$

where the individual limits are set to the following values in accordance to the operating ranges observed in experimental responses [33]: $T_{cab,\max} = 20\ ^\circ\mathrm{C}$, $T_{clnt,\max} = 90\ ^\circ\mathrm{C}$, $T_{in,\max} = 60\ ^\circ\mathrm{C}$, $\dot{V}_{p,\min} = 2$ L/min, $\dot{V}_{p,\max} = 30$ L/min, $\dot{V}_{bf,\min} = 50\ \mathrm{m^3/h}$, $\dot{V}_{bf,\max} = 250\ \mathrm{m^3/h}$, $P_{PTC,\max} = 5$ kW.

The state and control variable constraints (17a–e) are imposed as hard constraints, by iterating within the DP algorithm only over the specified control variable range and

discarding solutions that violate the state constraints. The final condition (16) and the inlet temperature–output constraint (17f) are accounted for by extending the cost function (14):

$$J = J_f(T_{cab}(N_t)) + \sum_{k=0}^{N_f-1} [P_{HVAC}(k)\tau_s + K_{lim}(H(T_{in}(k) - T_{in,\max}))], \tag{18}$$

where the final condition-related term $J_f$ is given by

$$J_f = \begin{cases} K_f(T_{cab,f} - T_{cab}(N_f))^2, & \text{if } T_{cab}(N_f) \le T_{cab,f}, \\ 0, & \text{otherwise}, \end{cases} \tag{19}$$

with the penalization factor $K_f$ set to a relatively high value ($K_f = 10^{12}$, herein) to ensure satisfaction of the terminal condition. Note that for numerical reasons the penalization narrows to the case of the end temperature $T_{cab}\left(N_f\right)$ being lower than the target one $T_{cab,f}$, while the opposite, the temperature excess case, is handled implicitly through the energy minimization term of the cost function (18). The second term within the summation parentheses in the cost function (18) represents a soft constraint related to the inequality condition (17f), where the Heaviside function $H(.)$ is defined as

$$H(k) = \begin{cases} 1, & \text{for } k \ge 0, \\ 0, & \text{for } k < 0, \end{cases} \tag{20}$$

while the weighting factor $K_{lim}$ is set to a sufficiently high value (equal to $K_f$, herein) to satisfy the constraint.

In the DP algorithm implementation, the state and control variables are uniformly discretized into a certain number of steps, $N_{(.)}$, in between the lower and upper limits defined by Equation (17). It is found by a trial-and-error approach that the setting $N_{T_{clnt}} = 50$, $N_{T_{cab}} = 2001$, $N_{\dot{V}_{bf}} = 15$, $N_{\dot{V}_p} = 15$, $N_{PTC} = 41$, with the time step (i.e., sampling period) being $\tau_s = 50$ s, provides favorable optimization accuracy and affordable computing efficiency. The DP optimization was implemented in the MATLAB environment and run on a workstation equipped with an Intel® Core™ i7-7700HQ processor (2.80 GHz) and 16 GB of RAM, resulting in a computation time of 4763 s. For comparison, the computation time can be reduced to 115 s by employing a significantly coarser discretization grid ($N_{T_{clnt}} = 10$, $N_{T_{cab}} = 2001$, $N_{\dot{V}_{bf}} = 10$, $N_{\dot{V}_p} = 10$, $N_{PTC} = 10$, $\tau_s = 50$ s), at the expense of only around a 2% increase in the resulting energy consumption. The cabin temperature discretization step $N_{T_{cab}}$ has been found to be the most influential due to the numerical sensitivity to handling the large terminal term penalty within (19) when executing the backward propagation phase of the algorithm.

### *3.2. Optimization Results*

DP optimization is conducted over the heat-up interval $t_f = 4000$ s for the final condition $T_{cab,f} = 18$ °C, which is achievable by the control allocation strategy (see Section 7). The initial conditions are set to ambient temperature: $T_{cab}(0) = T_{clnt}(0) = T_{amb} = 0$ °C.

The optimization results shown in Figure 6, with the emphasis on PTC heater power response $P_{PTC}$, point out that DP postpones heating for a period of 300 s, meaning that the heat-up interval can be shorter than 4000 s. Figure 7 shows the corresponding individual HVAC actuator power responses and related charts of the optimized points plotted over the actuator power consumption maps from Figure 2. The latter reveals that, while the blower fan operates mostly at the maximum volumetric flow $\dot{V}_{bf,\max}$, the optimizer predominantly sets the pump operating points around the knee of the respective power consumption map.

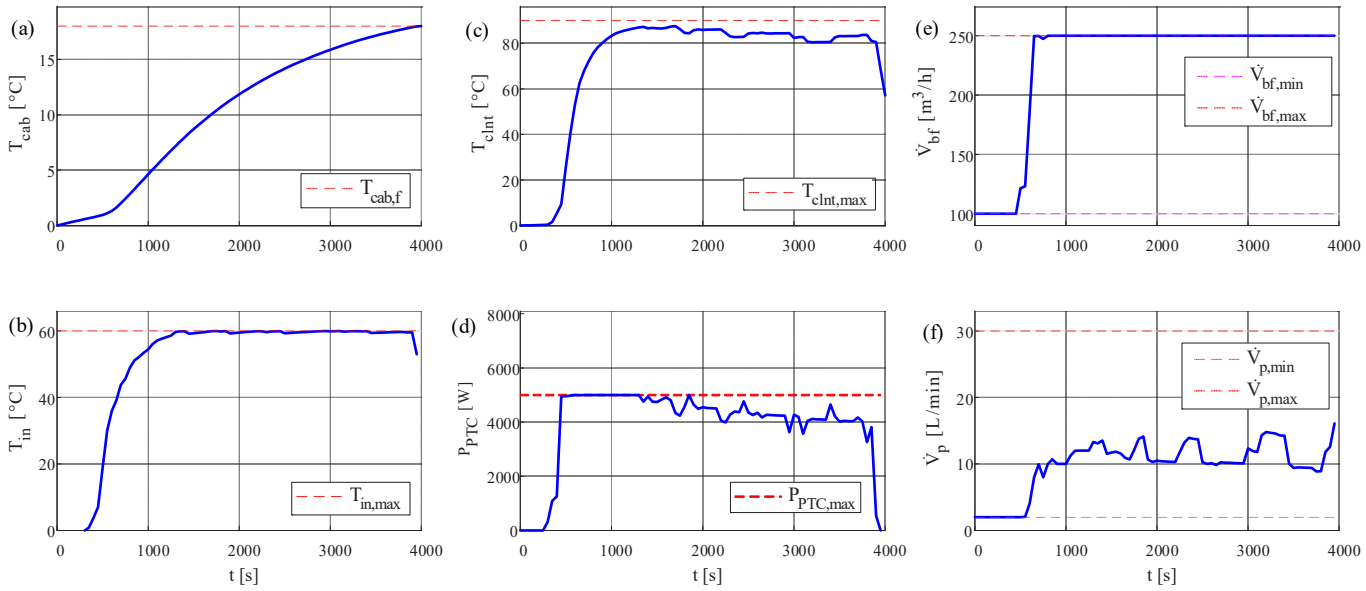



**Figure 6.** DP-optimized heat-up time responses of HVAC system (described by reduced-order model).

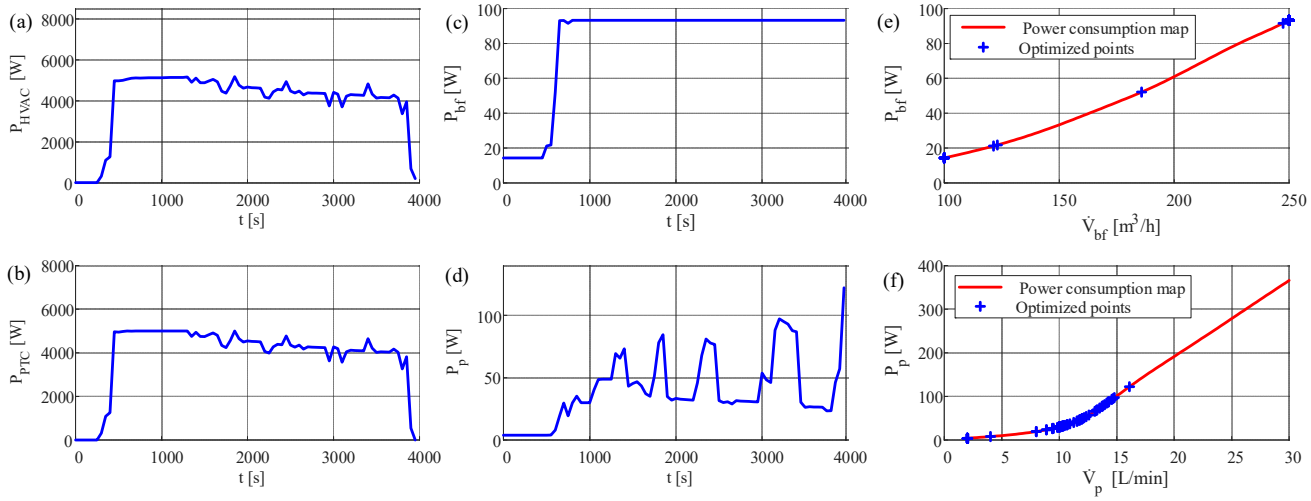



**Figure 7.** DP-optimized individual power consumption time responses (**a**–**d**) and respective samples plotted over actuator power consumption maps (**e**–**f**).

To gain further insights into optimal HVAC operation, zoom-in details of Figure 6 are extracted in Figure 8 and further analyzed. The blower fan is activated 200 s later than the PTC heater (at $t$ = 500 s), and the pump activation is delayed for an additional 100 s (at $t$ = 600 s), which is apparently to heat up the coolant first for reduced energy consumption. Furthermore, it can be observed that all control inputs are increased gradually. The plots of optimized control input samples versus the optimal cabin inlet temperature samples are shown in Figure 9. They indicate that the blower fan and pump flows (Figure 9a,b) can be related to the inlet temperature, which is a useful insight for the design of the rule-based control strategy presented in Section 4.

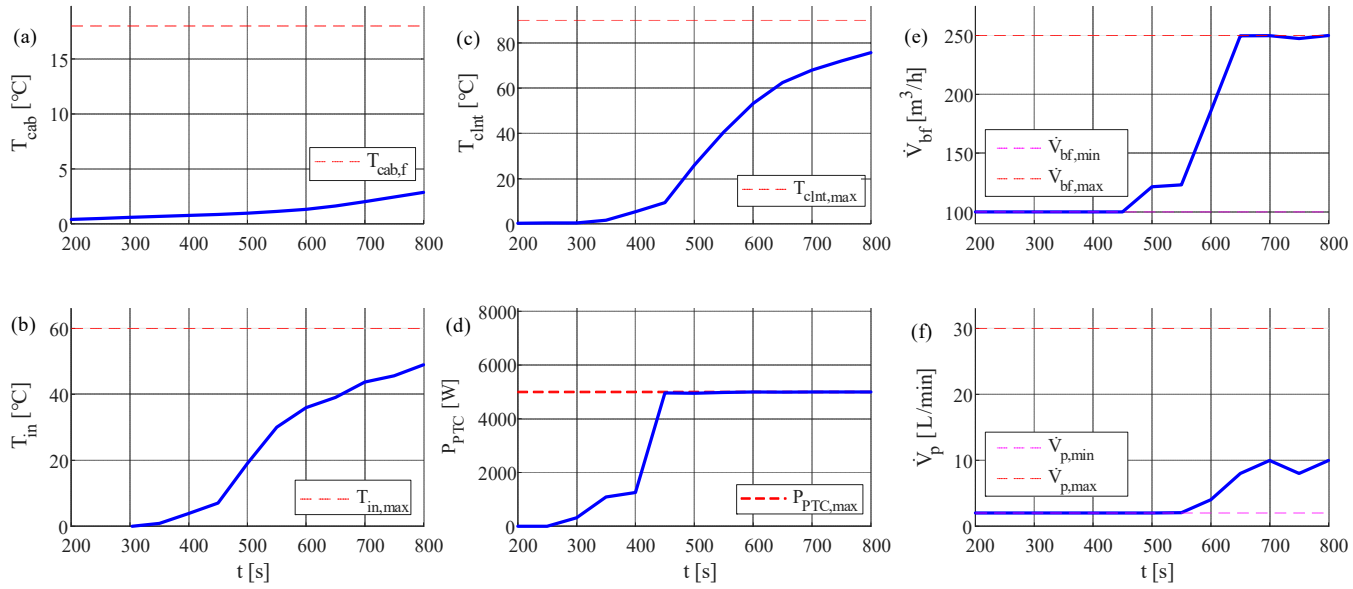



**Figure 8.** Zoom-in detail of response from Figure 6.

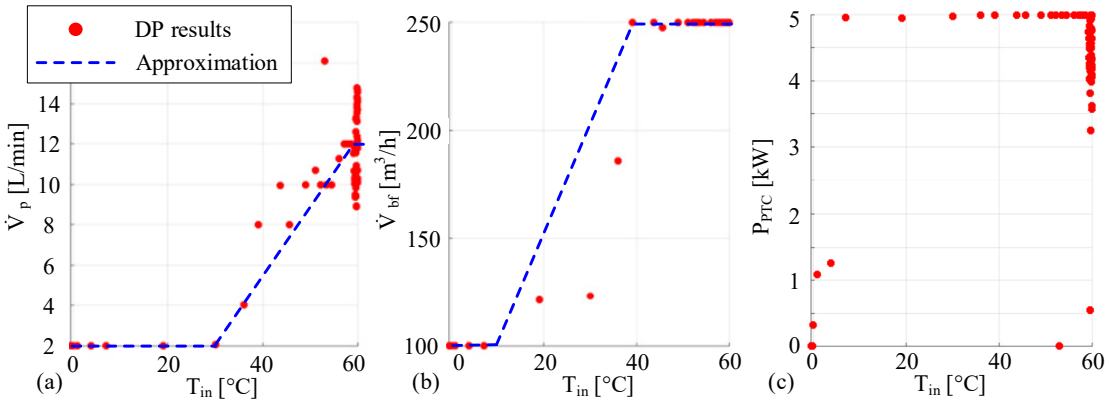



**Figure 9.** DP-optimized control input samples vs. optimal cabin inlet temperature samples, and related approximations used in rule-based control strategy.

## 4. HVAC Control

After overviewing the structure of the overall control system, this section elaborates on the design of the control allocation strategy, including corresponding rule-based and low-level controllers.

### *4.1. Overview of Control System Structure*

The proposed hierarchical control system is described by the structural block diagram shown in Figure 10 (see the Nomenclature Section for the definition of the system variables). The control strategy consists of (i) a superimposed PI cabin temperature controller that outputs the heating power demand $\dot{Q}_{h,R}$, (ii) optimal control allocation maps that coordinate the individual actuators, and (iii) a low-level cabin inlet air temperature PI controller that commands the PTC heater power $P_{HVAC}$. Based on the demanded heating power $\dot{Q}_{h,R}$ and the cabin temperature $T_{cab}$, the control allocation determines the cabin inlet air temperature reference $T_{in,R}$, as well as the air blower fan and coolant pump volume flow commands $\dot{V}_{bf}$ and $\dot{V}_{p}$, respectively. The blower fan and pump inputs are applied directly to the corresponding actuators (open-loop control), while $T_{in,R}$ is fed to the corresponding low-level PI-type feedback controller. In application, the pump and blower open-loop controls can typically be replaced by actuator-maps-based closed-loop interventions to compensate

for disturbance effects such as pressure drops, temperature-dependent properties (e.g., density variations), and component wear. The ambient condition disturbance vector **d** includes the ambient temperature $T_{amb}$ and the vehicle velocity $v_{veh}$, which are set to constant values of 0 °C and 50 km/h, respectively. To limit the coolant temperature in the absence of an explicit/cascaded coolant temperature controller, a P controller-like safety mechanism is designed. Details of the design of individual control subsystems are given in the next subsections, with the exception of the superimposed cabin temperature controller, whose design is presented in Section 5.

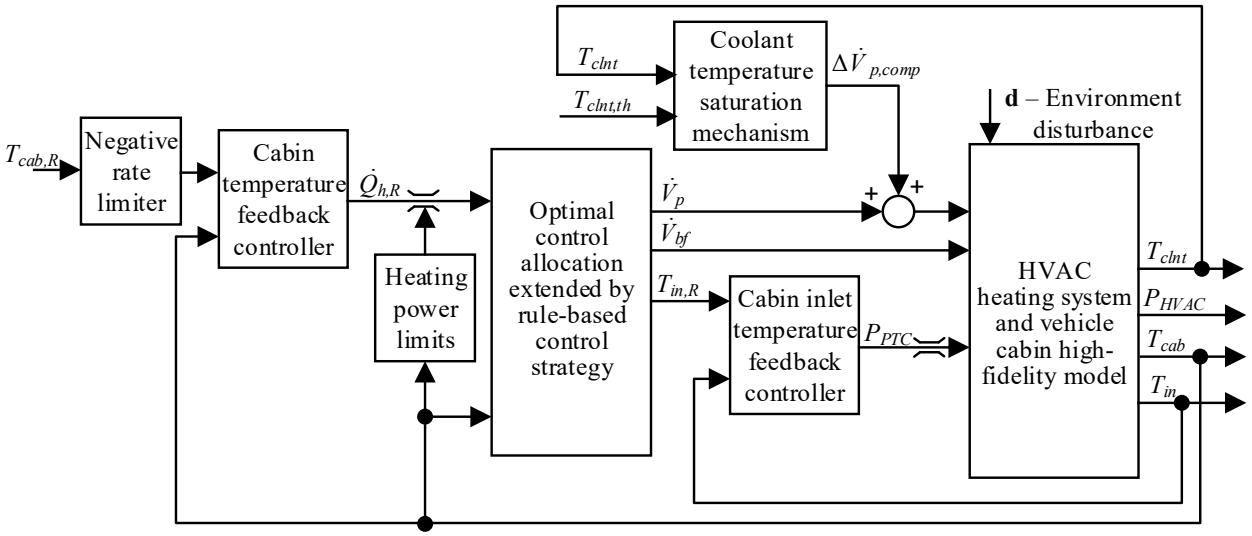



**Figure 10.** Structural block diagram of overall hierarchical minibus cabin heating control system.

### *4.2. Optimal Control Allocation Maps*

#### 4.2.1. Optimization Dataset

According to Figure 10, the optimal control allocation maps transform the heating power demand $\dot{Q}_{h,R}$ and the cabin temperature $T_{cab}$ to low-level controller inputs. Since the $T_{cab}$ dynamics are slow relative to those of the HVAC system state variable $T_{clnt}$ and $T_{in}$ (see Figure 5 for the worst-case heat-up scenario), the relatively detailed and complex cabin thermal dynamics model (Figure 3) can be excluded from the allocation maps optimization, i.e., a computationally efficient instantaneous optimization procedure can be applied based on constant boundary conditions for $T_{cab}$ (and $RH_{cab}$) [12]. It should be noted that such a control allocation approach ensures optimal control only in (quasi-) steady-state conditions, i.e., where the inlet air temperature $T_{in}$ is relatively close to its reference $T_{in,R}$. During pronounced transients, such as those during the initial system heat-up period, the inlet temperature $T_{in}$ can significantly differ from its reference $T_{in,R}$, thus leading to generally suboptimal control allocation.

To derive the optimal allocation maps, a grid-search optimization method was employed. Firstly, extensive automated simulations were performed by using the high-fidelity HVAC system model, with enough time left for the system to reach stationary conditions. Each operating condition was simulated up to $t_f = 2000$ s to allow sufficient time to reach the steady-state condition, where the particular end time $t_f$ was determined conservatively based on a visual inspection of characteristic system responses. The relevant simulation outputs, stored for the grid-search algorithm, include the total power consumption $P_{HVAC}$, the inlet air temperature $T_{in}$, the coolant temperature $T_{clnt}$ and the heating power $\dot{Q}_h = \dot{V}_{bf}\rho_{cab}c_{p,cab}(T_{in} - T_{cab})$ (see Equation (5)). The simulations were performed for a wide and dense grid of control inputs, defined in Table 1, and for the fixed cabin temperature values $T_{cab} \in [0:5:20]$ °C.

**Table 1.** Control input simulation grid applied when generating optimization dataset.

| Actuator Grid Resolution and Imposed Limits |
|---|
| $P_{PTC} = [500 : 250 : 5000]$ W |
| $\dot{V}_{bf} = [50 : 50 : 250]$ m$^3$/h |
| $\dot{V}_p = [2 : 2 : 30]$ L/min |

4.2.2. Optimization

A grid-search algorithm is executed over the prepared optimization dataset to identify the optimal actuator combinations that minimize the total power consumption:

$$J_{CA} = \min(P_{HVAC}) = \min\left(P_{PTC} + P_{bf} + P_p\right), \tag{21}$$

for different sets of cabin temperature $T_{cab}$ and heating power demand $\dot{Q}_{h,R}$ while accounting for the following operational constraints:

$$30 \leq T_{in}[^\circ\text{C}] \leq 60, \tag{22a}$$

$$T_{clnt}\ [^\circ\text{C}] \leq 90. \tag{22b}$$

The optimization algorithm is given below as Algorithm 1. It firstly linearly interpolates the outputs $T_{in}$, $T_{clnt}$, $\dot{Q}_h$, and $P_{HVAC}$ to a high resolution of $80 \times 80$ equally spaced points $(\dot{V}_{p,grid}, \dot{V}_{bf,grid})$ (finer than in Table 1). For each grid point, the corresponding $P_{PTC}$ required to make the heating power $\dot{Q}_h = c_{p,cab}\rho_{cab}\dot{V}_{bf}(T_{in} - T_{cab})$ equal to its demand $\dot{Q}_{h,R}$ is found. Each candidate triple $(\dot{V}_p, \dot{V}_{bf}, P_{PTC})$ is then checked against operational constraints (22), as well as the constraint $P_{PTC,\min} \leq P_{PTC} \leq P_{PTC,\max}$, and a feasible point yielding the minimum total power $P_{HVAC}$ (see Equation (2)) is stored as the optimal result. If no feasible point exists, which typically occurs when $\dot{Q}_{h,R}$ is outside the system limits, a second, fallback routine is activated, where the discrepancy between the demanded and achieved $\dot{Q}_h$ is minimized, while satisfying the operational constraints. Figure 11 shows the achieved maximum (limit) values of HVAC heating power $\dot{Q}_h$, which are reconstructed from the triples $(\dot{V}_p, \dot{V}_{bf}, P_{PTC})$ stored against operating points $(T_{cab}, \dot{Q}_{h,R})$ and used to saturate the superimposed controller (Figure 10). The lower saturation limit of 1000 W (Figure 11) is set to satisfy the lower constraint of Equation (22a).

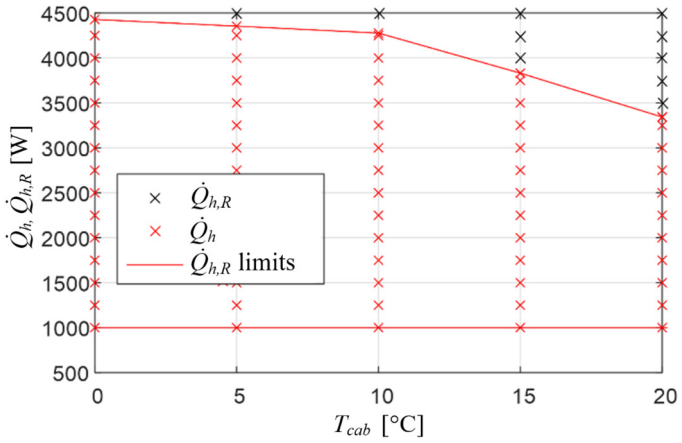



**Figure 11.** Illustration of determining HVAC system heating power limits in dependence on cabin temperature.

**Algorithm 1.** Grid-Search Algorithm

FOR each cabin temperature $T_{cab} \in \{0,\ 5,\ 10,\ 15,\ 20\}$ °C:
- From dataset build linear interpolant functions of output allocation variables: $f_{\dot{Q}_h}(\dot{V}_p, \dot{V}_{bf}, P_{PTC})$, $f_{P_{HVAC}}(\dot{V}_p, \dot{V}_{bf}, P_{PTC})$, $f_{T_{in}}(\dot{V}_p, \dot{V}_{bf}, P_{PTC})$, $f_{T_{clnt}}(\dot{V}_p, \dot{V}_{bf}, P_{PTC})$

FOR each target heating level $\dot{Q}_{h,R} \in \{1000,\ 1250,\ 1500,\ \ldots,\ 4500\}$ W:
- $P^*_{HVAC}$ = Inf //Initializing optimal/minimal power consumption
- FOR each point in $(\dot{V}_{p,grid}, \dot{V}_{bf,grid})$:
  - Find $P_{PTC}$ that minimizes $|\dot{Q}_{hR} - f_{\dot{Q}_h}(\dot{V}_p, \dot{V}_{bf}, P_{PTC})|$
  - Check if point $(\dot{V}_p, \dot{V}_{bf}, P_{PTC})$ satisfies:
    - $P_{PTC,\min} \le P_{PTC} \le P_{PTC,\max}$
    - $T_{in,\min} \le f_{T_{in}}(\dot{V}_p, \dot{V}_{bf}, P_{PTC}) \le T_{in,\max}$
    - $f_{T_{clnt}}(\dot{V}_p, \dot{V}_{bf}, P_{PTC}) \le T_{clnt,\max}$
  - IF point satisfies constraints AND $P_{HVAC} < P^*_{HVAC}$
    - $P^*_{HVAC} = P_{HVAC}$
    - Store $(\dot{V}_p, \dot{V}_{bf}, P_{PTC})$
- IF no feasible point is found: //Find feasible point minimizing $|\dot{Q}_{hR} - \dot{Q}_h|$
  - $\Delta\dot{Q}^*_{hR}$ = Inf //Initialization
  - FOR each point in $(\dot{V}_{p,grid}, \dot{V}_{bf,grid})$:
    - FOR $P_{PTC}$ grid
      - Check feasibility
        - $T_{in,\min} \le f_{T_{in}}(\dot{V}_p, \dot{V}_{bf}, P_{PTC}) \le T_{in,\max}$
        - $f_{T_{clnt}}(\dot{V}_p, \dot{V}_{bf}, P_{PTC}) \le T_{clnt,\max}$
      - Evaluate $\Delta\dot{Q}_{hR} = |\dot{Q}_{hR} - f_{\dot{Q}_h}(\dot{V}_p, \dot{V}_{bf}, P_{PTC})|$
      - IF point is feasible AND $\Delta\dot{Q}_{hR} < \Delta\dot{Q}^*_{hR}$
        - $\Delta\dot{Q}^*_{hR} = \Delta\dot{Q}_{hR}$
        - Store $(\dot{V}_p, \dot{V}_{bf}, P_{PTC})$

#### 4.2.3. Control Allocation Maps

The obtained optimal allocation maps are shown in Figure 12 for the considered range and quantization of inputs $\dot{Q}_{h,R}$ and $T_{cab}$. Exceptionally, the quantization level of $\dot{Q}_{h,R}$ is lower than the prescribed value of 250 W for the highest $\dot{Q}_{h,R}$ point (highlighted by a yellow circle and corresponding to the upper limit from Figure 11). Figure 12d indicates that the PTC heater power $P_{PTC}$ rises approximately linearly with the heating power demand $\dot{Q}_{h,R}$, and its allocation is relatively insensitive to the cabin temperature $T_{cab}$. Figure 12c,e show the resulting coolant and cabin inlet air temperatures, $T_{clnt}$ and $T_{in}$, which satisfy the limits defined by inequalities (22). At lower values of $T_{cab}$, $T_{in}$ is mostly saturated at its lower limit and it reaches the upper limit only at the highest heating power demand points. Figure 12b indicates that the air blower fan flow $\dot{V}_{bf}$ is generally allocated toward the upper end of the operating range, particularly for higher values of $T_{cab}$. To maintain the commanded $\dot{Q}_{h,R}$ when $T_{in}$ is saturated at the lower limit, the flow $\dot{V}_{bf}$ increases linearly, and once it reaches the upper limit, $T_{in}$ rises accordingly (see Equation (5)). Conversely, the coolant pump flow rate $\dot{V}_p$ is mostly allocated at the lower end of the operating range, increasing only at the points of maximum heating power demand (Figure 12a). This solution reflects the optimal allocation tendency to minimize the actuator losses and, thus, minimize the overall energy consumption, as discussed in more detail in Section 7.

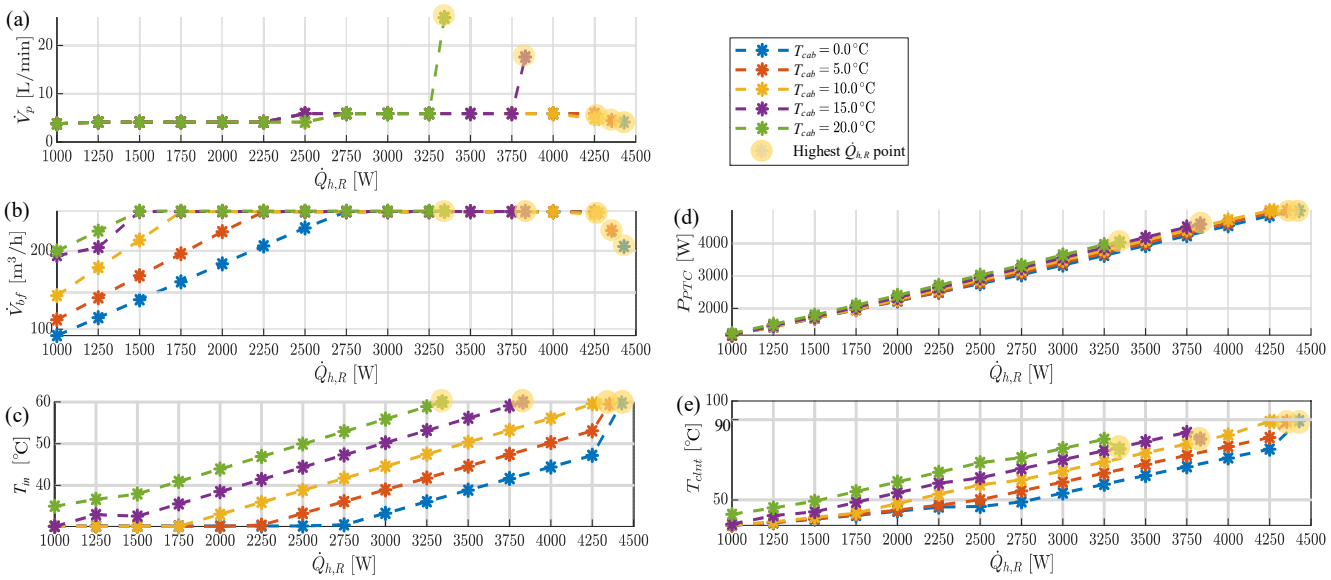



**Figure 12.** Optimized allocation maps (**a**–**c**) and related HVAC variables (**d**,**e**).

The obtained optimal control allocation results in Figure 12a–c are directly implemented within the control strategy shown in Figure 10 as lookup tables (maps). Alternatively, the allocation maps could be approximated by analytical expressions as demonstrated in [12].

Sensitivity of the optimal allocation maps has also been verified with respect to the HVAC system unmodeled dynamic effects, including: (i) variation of cabin-to-HVAC system recirculation air temperature $T_{rec}$ from Figure 1, where $T_{rec} > T_{cab}$ holds due to the distributed nature of the minibus cabin thermal model (Figure 3), and (ii) deviations in ambient temperature relative to the nominal condition $T_{amb} = 0$ °C. To assess the influence of these effects, the allocation maps were reoptimized for $T_{rec} = T_{cab} + 5$ °C and $T_{amb} \in \{-10,\ 10\}$ °C, and the results were compared with those obtained under the nominal scenario ($T_{rec} = T_{cab}$, $T_{amb} = 0$ °C). Only minor differences in the total energy consumption have been observed, thus indicating low sensitivity of the allocation approach.

### *4.3. Low-Level Control*

#### 4.3.1. HVAC System Model

The low-level PI controller aims to provide accurate tracking of the cabin air inlet temperature reference $T_{in,R}$ and effective disturbance rejection (e.g., when manipulating the pump flow control input). For the sake of analytical controller parameter optimization, the HVAC model is linearized and represented by a second-order lag term, extended with a pure delay associated with the coolant transport pipe length:

$$G_p(s) = \frac{T_{in}(s)}{P_{PTC}(s)} = \frac{K_{P1}}{(\tau_{P1}s + 1)(\tau_{P2}s + 1)} e^{-\tau_d s}. \tag{23}$$

The slow time constant ($\tau_{P1}$) corresponds to PTC heater-to-coolant heat transfer. On the other hand, the fast time constant ($\tau_{P2}$) corresponds to heat transfer from the coolant to the inlet air via the heater core.

The identified numerical values of the time constants and the gain of the transfer function (23) are shown in Figure 13 for different operating points used in the optimization study in Section 4.2. The time constants are obtained by using the MATLAB function *tfest(.)* applied to system step responses (for $P_{PTC}$ step of approximately 5% of the maximum PTC power; small-signal operating mode to which the linear model applies). The corresponding

correlation indices, shown in the same figure, indicate that the slow time constant $\tau_{P1}$ and the system gain $K_{P1}$ are strongly correlated with the blower flow ($r = -0.96$ on a scale from 0 to $\pm 1$), while the fast time constant $\tau_{P2}$ correlates well with the pump flow ($r = -0.69$). The pure delay $\tau_d$ primarily depends on the coolant pump flow, and it ranges from approximately 3 to 4.5 s with the correlation coefficient $r = -0.71$.

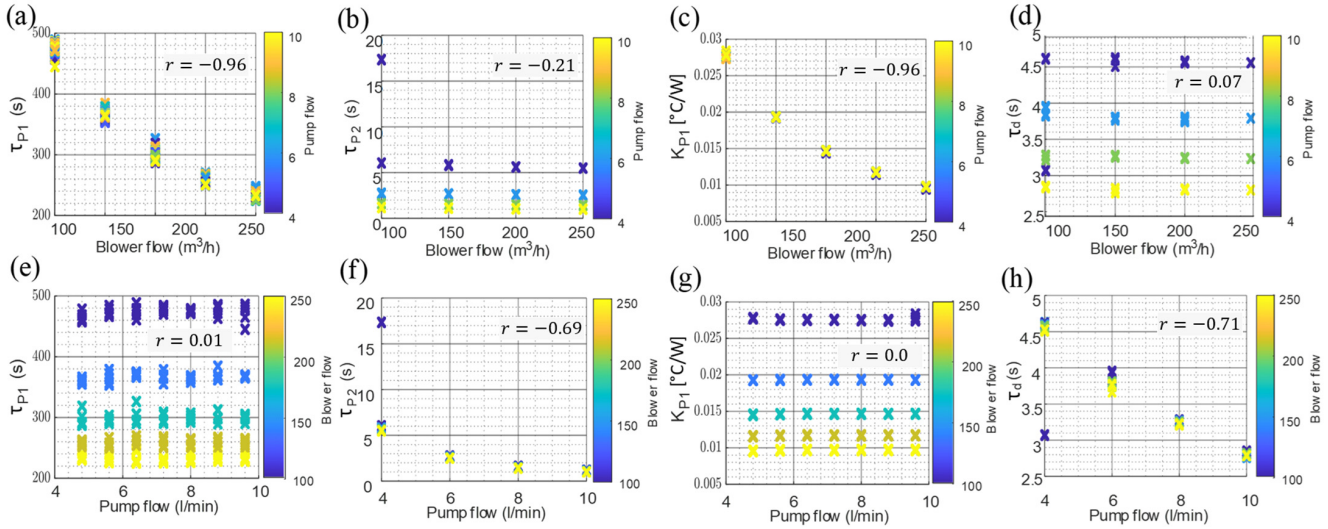



**Figure 13.** Identified parameters of process in low-level control system and respective correlation coefficients with respect to given $x$-axis variable.

One may assume that owing to a strong control effort, the closed-loop system would be much faster than the open-loop response dominated by the slow time constant $\tau_{P1}$. Consequently, the second-order lag term may be simplified to a series connection of integral and first-order lag term, for which the analytical optimal solution for PI controller parameters exists (symmetrical optimum, [35]):

$$G_p'^{(s)} = \frac{T_{in}(s)}{P_{PTC}(s)} = \frac{K_P}{(\tau_{P1}s+1)(\tau_{P2}s+1)} e^{-\tau_d s} \approx \frac{\frac{K_P}{\tau_{P1}}}{s(\tau'_{P2}s+1)} = \frac{K_P\prime}{s(\tau'_{P2}s+1)}, \quad (24)$$

where the equivalent lag time constant $\tau'_{P2}$ also accounts for pure delay $\tau_d$ ($\tau'_{P2} = \tau_{P2} + \tau_d$). This time constant is conservatively set to the upper edge of identified values from Figure 13 ($\tau'_{P2} = 10$ s). Another advantage of the process model simplification is that the integral gain $K'_P = K_P/\tau_{P1}$ is found to be rather independent of the process operating point (unlike the individual parameters $K_P$ and $\tau_{P1}$, see Figure 13), thus avoiding the need for controller adaptation (i.e., gain scheduling).

#### 4.3.2. Controller Tuning and Verification

The symmetrical optimum solution for the parameters of the PI controller

$$G_{PI,in}(s) = \frac{P_{PTC}(s)}{T_{in,R}(s) - T_{in}(s)} = K_{p,in}\frac{\tau_{i,in}s+1}{\tau_{i,in}}, \quad (25)$$

and the simplified process model (25) is as follows [35,36]:

$$K_{P,in} = \frac{2}{K_P\prime\tau_e}, \quad (26a)$$

$$\tau_{i,in} = \tau_e, \quad (26b)$$

$$\tau_{P1}/\kappa = \tau_{e,\max} \geq \tau_e \geq \tau_{e,\min} = 4\tau'_{P2}. \quad (26c)$$

The solution provides a fast and well-damped (so-called quasi-aperiodic) response, with the fastest (theoretically optimal) response obtained for the equivalent closed-loop system time constant $\tau_e$ set to $\tau_{e,\min}$. However, to reduce the control effort and sensitivity to noise and process unmodeled dynamics, one may arbitrarily increase $\tau_e$ up to $\tau_{e,\max}$, which should be distant enough from the slow process time constant ($\kappa \cong 5$ in Equation (26c)) to satisfy the assumption in the description of the integral+lag process dynamics (24). On the other hand, it can be shown through simulation that the energy consumption is barely affected by the selection $\tau_e$.

The controller tuned for the simplified linear process model has been verified on the high-fidelity nonlinear HVAC model. The corresponding closed-loop system responses are shown in Figure 14 for the equivalent time constant tuned for the fastest response, $\tau_e = \tau_{e,\min} = 4\tau'_{P2} = 40$ s, and for different coolant pump speeds, air blower flows, and cabin temperature operating points. A realistic inlet temperature measurement noise is considered in the high-fidelity simulation model. The small-signal operating mode responses are fast and well-damped for different operating points (see the detail of the response shown in the right-hand column of Figure 14a). The fast response (much faster than the open-loop response) is owing to a strong control effort related to selection of a fast equivalent time constant $\tau_e \ll \tau_{P1}$ (see Figure 14b). The first part of the response in Figure 14 (up to 700 s) indicates that the system behavior is favorable in the large-signal operating mode as well. Here, the response time is dictated by the PTC heater power limit (set to 5000 W) and the operating point. The noise sensitivity is small (no notable noise in the commanded signal $P_{PTC}$).

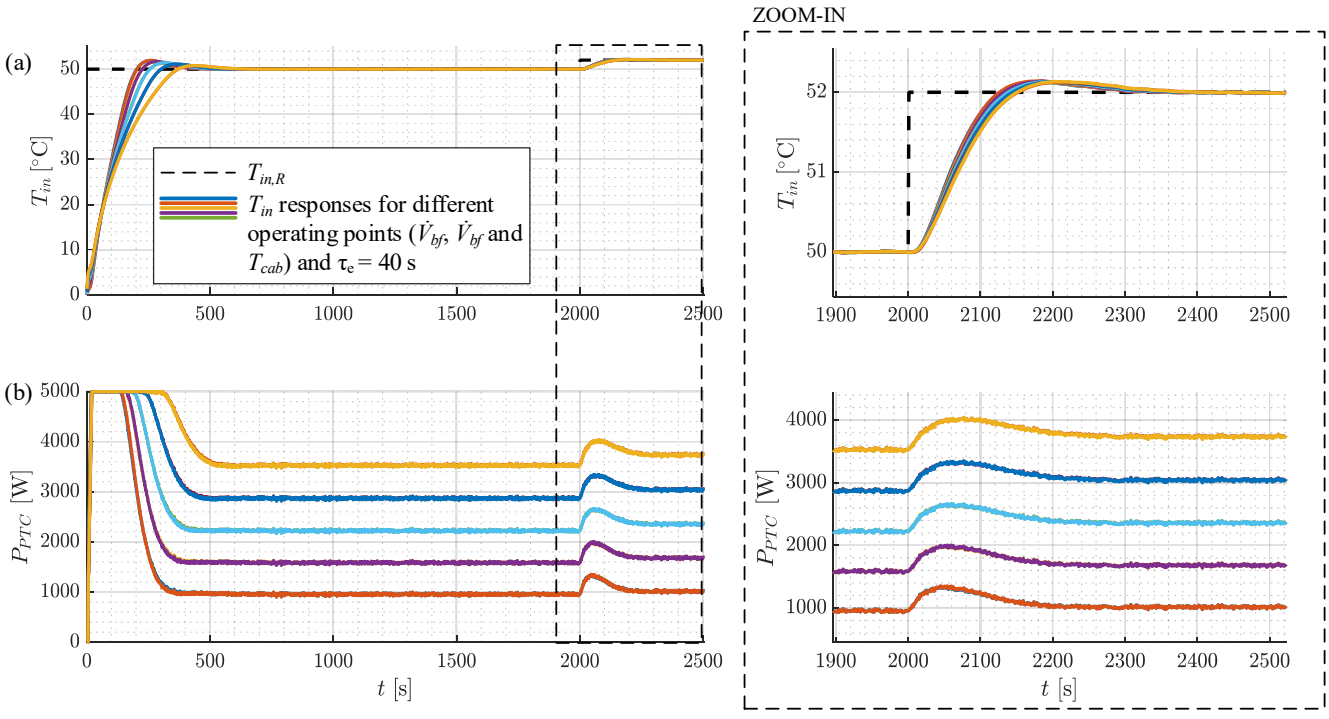



**Figure 14.** Responses of the low-level closed-loop system involving the high-fidelity process model at different operating points.

#### 4.3.3. Coolant Temperature Safety Mechanism

The PI controller of cabin air inlet temperature $T_{in}$ cannot guarantee that the upper limit (22b) of the coolant temperature $T_{clnt}$ is met. Namely, although the optimal allocation accounts for the constraint (22b), in the large-signal operating mode transients the coolant temperature could exceed its limit. A potential solution could be to incorporate an inner

controller of coolant temperature, but such a cascade control system would be more complex to tune and generally slower than the single-level controller-based one. Therefore, a simpler safety mechanism is proposed in Figure 10, which increases the pump flow in proportion to coolant temperature excess $T_{clnt} - T_{clnt,th}$, where the threshold $T_{clnt,th}$ is conservatively set somewhat below the target temperature limit of 90 °C from Equation (22b) (to 85 °C, herein):

$$\Delta\dot{V}_{p,comp} = \begin{cases} K_{comp}(T_{clnt} - T_{clnt,th}), & \text{for } T_{clnt} > T_{clnt,th} \\ 0, & \text{for } T_{clnt} \leq T_{clnt,th} \end{cases}. \quad (27)$$

### *4.4. Control Trajectory Optimization-Inspired Rule-Based Control Strategy*

The insights obtained through the DP control trajectory optimization results presented in Section 3 for the heat-up transient scenario can be summarized as follows:

1. Control variables $P_{PTC}$, $\dot{V}_{bf}$, and $\dot{V}_p$ increase gradually toward their quasi-stationary values (Figure 8), with $P_{PTC}$ and $\dot{V}_{bf}$ tending toward their maximum values, while $\dot{V}_p$ reaches values on the knee of the corresponding power consumption characteristic (Figure 7).
2. The rise in the blower fan flow $\dot{V}_{bf}$ is delayed with respect to PTC power $P_{PTC}$, while the pump flow $\dot{V}_p$ is further delayed with respect to blower fan flow $\dot{V}_{bf}$ (Figure 8).
3. The blower fan and pump flows, $\dot{V}_p$ and $\dot{V}_{bf}$, can be closely related to the inlet cabin air temperature $T_{in}$ (Figure 9a,b).
4. The inlet temperature $T_{in}$ is kept around its limit value $T_{in,max}$, while $P_{PTC}$ is adjusted by the inner inlet temperature controller (Figure 6).

A simple rule-based (RB) control strategy, inspired by the DP optimization results summarized above, has been designed for heat-up transient conditions, i.e., until approaching the target cabin temperature. The RB strategy employs the same $T_{in}$ PI controller as shown in Figure 10, but sets its reference to the maximum inlet temperature $T_{in,R} = T_{in,\max}$. The blower fan and pump flow control inputs are set in dependence on the actual inlet temperature $T_{in}$ (see the piecewise-linear approximations in Figure 9):

$$\dot{V}_{bf} = \begin{cases} \dot{V}_{bf,\min}, & \text{for } T_{in} < T_{in,bf,1} \\ \dot{V}_{bf,\min} + \frac{T_{in} - T_{in,bf,1}}{T_{in,bf,2} - T_{in,bf,1}}(\dot{V}_{bf,\max} - \dot{V}_{bf,\min}), & \text{for } T_{in,bf,1} \leq T_{in} \leq T_{in,bf,2} \\ \dot{V}_{bf,\max}, & \text{for } T_{in} > T_{in,bf,2} \end{cases} \quad (28)$$

$$\dot{V}_p = \begin{cases} \dot{V}_{p,\min}, & \text{for } T_{in} < T_{in,p,1} \\ \dot{V}_{p,\min} + \frac{T_{in} - T_{in,p,1}}{T_{in,p,2} - T_{in,p,1}}(\dot{V}_{p,knee} - \dot{V}_{p,\min}), & \text{for } T_{in,p,1} \leq T_{in} \leq T_{in,p,2} \\ \dot{V}_{p,knee}, & \text{for } T_{in} > T_{in,p,2} \end{cases} \quad (29)$$

with $T_{in,bf,1} = 10$ °C, $T_{in,bf,2} = 40$ °C, $T_{in,p,1} = 30$ °C, $T_{in,p,2} = 60$ °C. The pump flow parameter $\dot{V}_{p,knee}$ is set to 12 L/min as an approximate mean value of the DP pump flows after reaching quasi-stationary conditions (see the final cloud of dots in Figure 9a). Note that introducing the thresholds $T_{in,bf,1}$ and $T_{in,p,1}$ gives the effect of initially delayed fan and pump responses (with respect to the $P_{PTC}$ response, Point 2 above), with the pump activation delay being larger than that of the fan due to $T_{in,p,1} > T_{in,bf,1}$.

The proposed RB strategy is intended exclusively for the heat-up transient operating phase. It remains active until the cabin temperature reaches its heat-up target value, after which the control system is switched to the CA strategy for optimal quasi-steady-state operation. The RB strategy is activated again when the cabin temperature falls below a threshold value that is distant enough from the regular cabin temperature reference value (i.e., a hysteresis is included between the RB strategy on and off thresholds).

## 5. Superimposed Cabin Temperature Control

This section elaborates on the design of the *Cabin temperature feedback controller* from Figure 10, which is superimposed to the core HVAC control system presented in Section 4. The design starts with identification of the structure and parameters of a linear process model, which are then used for controller numerical parameter optimization. The optimized controller is verified for both the linear model and the nonlinear high-fidelity model.

### *5.1. Process Identification*

The process in the superimposed cabin temperature control loop, comprising both the control-volume cabin model and the controlled HVAC system, is identified by using the output-error (OE) discrete-time model defined in the discrete-time Laplace (z) domain as

$$y(z) = z^{-n_k}\frac{B(z)}{F(z)}u(z) + e(z), \tag{30}$$

$$F(z) = 1 + f_1 z^{-1} + \cdots + f_{n_f} z^{-n_f},\ B(z) = b_0 + b_1 z^{-1} + \cdots + b_{n_b} z^{-n_b}, \tag{31}$$

where $y = T_{cab}$ and $u = \dot{Q}_{h,R}$ are the process output and input, respectively (see Figure 10), $B(z)$ and $F(z)$ are polynomials with free parameters to be identified, $n_f$ and $n_b$ are respective polynomial orders, $n_k$ is the number of pure delay steps, and $e(z)$ is the output disturbance term accounting for measurement noise.

The identification dataset is generated for multiple cabin temperature operating points, in which the system is excited by a chirp-type signal $u$ covering a broad band of frequencies and having an amplitude of about 2.5% of the maximum $\dot{Q}_{h,R}$ value for the linear/small-signal operating mode operation. The MATLAB system identification toolbox has been used to candidate the models of different orders, identify their parameters, and select the optimal model according to the Akaike information criterion [34]. The selected model is of the seventh order: $n_f = 7$, $n_b = 3$, and $n_k = 4$.

Variations in the linearized HVAC model parameters across the cabin temperatures in the range of interest (e.g., $T_{cab}$ [15,20] °C) are found not to be significant. Therefore, the controller parameters are fixed to those optimized for a single cabin temperature operating point: $T_{cab} = 18$ °C.

### *5.2. Controller Parameter Optimization*

A modified PI controller is used, where the proportional (P) term is relocated into the feedback path to reduce the step response overshoot. The controller parameters $K_{p,cab}$ and $\tau_{i,cab}$ are determined through numerical optimization, where the following cost function is defined to minimize the closed-loop control error, as well as the control effort [37]:

$$\min_{K_{p,cab},\tau_{i,cab}} J_{11} = \sum_{k=1}^{N_w} H(k-W)\left((T_{cab,R}(k) - T_{cab}(k))^2 + r\left(\frac{\dot{Q}_{h,R}(k)}{\dot{Q}_{h,Rs}} - 1\right)^2\right), \tag{32}$$

where $k$ is the sampling step (for the sampling time $\tau_s = 5$ s), $r$ is the weighting coefficient that sets the trade-off between the two criteria, $H(k)$ is the Heaviside function defined by (20), $W$ is the number of initial sampling steps for which the cost function is not evaluated (due to inevitably high control error in the initial period), and $\dot{Q}_{h,Rs}$ is the expected steady-state value of $\dot{Q}_{h,R}$.

The control error $T_{cab,R} - T_{cab}$ and the control variable $\dot{Q}_{h,R}$, are obtained as reference-step responses of the corresponding linear, discrete-time closed-loop transfer functions.

The optimization is conducted through a search algorithm implemented via the MATLAB function *fminsearch*(.).

In the first optimization run, both $W$ and $r$ are set to 0 to emphasize the response speed criterion. Then, the initial/masking time window $W$ is set to correspond to the rise time of the first-run cabin temperature step response ($H = 21$), resulting in damping of the response, while the weighting coefficient $r$ is adjusted to damp the residual response oscillations ($r = 0.05$).

### *5.3. Simulation Results*

Figure 15 shows the cabin temperature responses with respect to reference steps of 1 °C and 2 °C, where the overall control strategy from Figure 10 is involved and both high-fidelity and identified linear process models are considered. In the small-signal operating mode (i.e., for the reference step of 1 °C), the responses of the systems with the high-fidelity and linear models are very similar to each other (see Figure 15a,e). In contrast, for the higher reference step (2 °C), the response corresponding to the high-fidelity model (blue line) deviates from the linear behavior (dashed red line). This deviation primarily occurs because the inlet air temperature and pump flow reach saturation limits (large-signal operating mode; see Figure 15c,f). In the reference step-up case, the system response slows down as a result of saturation, but it remains stable and well damped. On the other hand, in the reference step-down case, the control input response reaches the lower saturation limit (Figure 15e), which significantly disturbs the coolant pump and air blower fan flow allocation (see the blue lines in Figure 15d,f). This is because the allocation was optimized for quasi-stationary conditions, and not for the abrupt transients occurring in this particular scenario. To make the operating conditions less abrupt for better allocation conditioning, a cabin temperature reference rate limiter is implemented in the direction of reference decrease. The reference decrease rate limit is set as a trade-off of response speed and damping (−0.05 °C/s, herein). The corresponding response in Figure 15 (solid orange line) indicates that applying the reference rate limiter significantly settles down the allocation responses and consequently dampens the cabin temperature and the heating power responses, without sacrificing the response settling time.

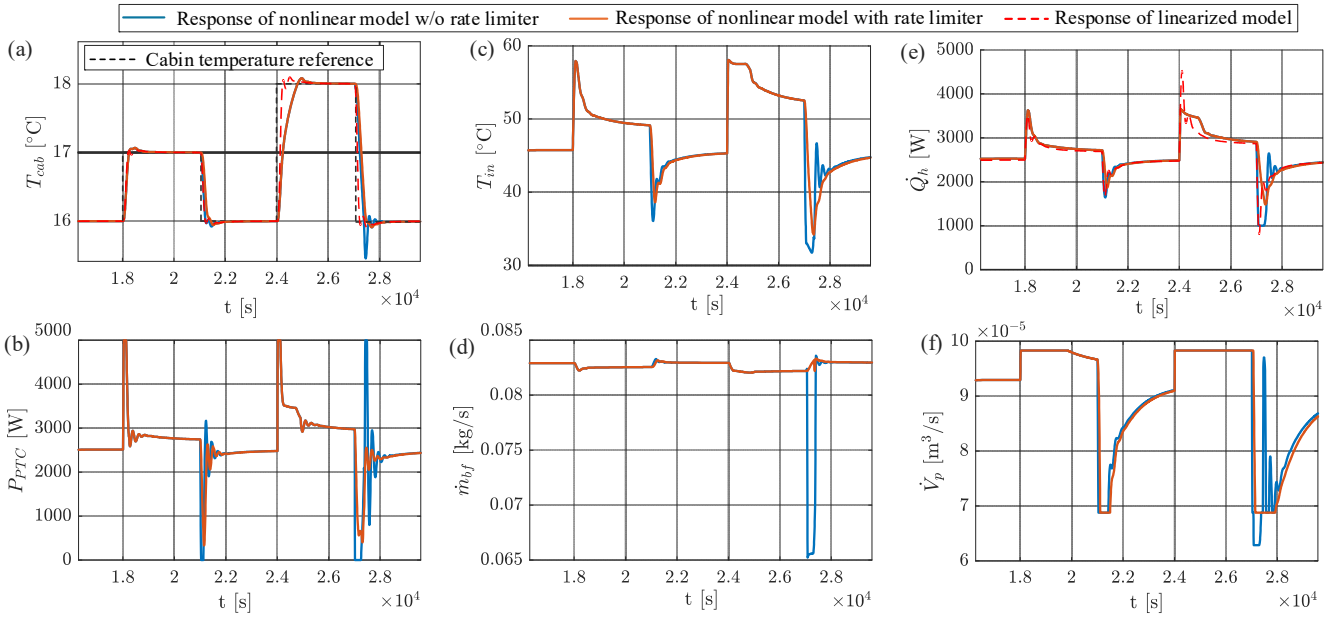



**Figure 15.** Step responses of overall hierarchical control strategy for nonlinear (high-fidelity) and identified linear process models.

## 6. Verification Against Industry Baseline

The proposed control allocation strategy has been verified against one reconstructed from real minibus data and experimental responses (denoted here as the industry baseline), where both strategies are linked to the same high-fidelity HVAC system model. The baseline strategy employs a PI controller for regulating the coolant temperature at a fixed value of 75 °C, while the pump speed and the blower flows are set to the fixed values of 250 $m^3/h$ and 18 L/min. In the comparative verification study, the cabin temperature is not feedback-controlled, i.e., the cabin thermal system operates in an open-loop mode. This is to ensure a fair comparison with the baseline strategy, which does not employ a cabin temperature controller. The verification relates to both stationary and highly transient (heat-up) conditions.

### *6.1. Stationary Conditions*

The stationary condition verification of the two strategies is based on the steady-state operating points used in the design of allocation maps. Thus, the cabin thermal model is omitted in this verification scenario, i.e., the cabin temperature $T_{cab}$ is treated as a fixed, prescribed operating point-related input rather than a feedback-controlled variable. The verification procedure first runs the industry baseline strategy for a given $T_{cab}$ (and the aforementioned fixed values of the coolant temperature reference and the pump and fan speeds), and the simulation-determined steady-state value $\dot{Q}_h$ is then used to select the corresponding point of the CA system (from the grid in Figure 12). The final comparative results are shown in Figure 16.

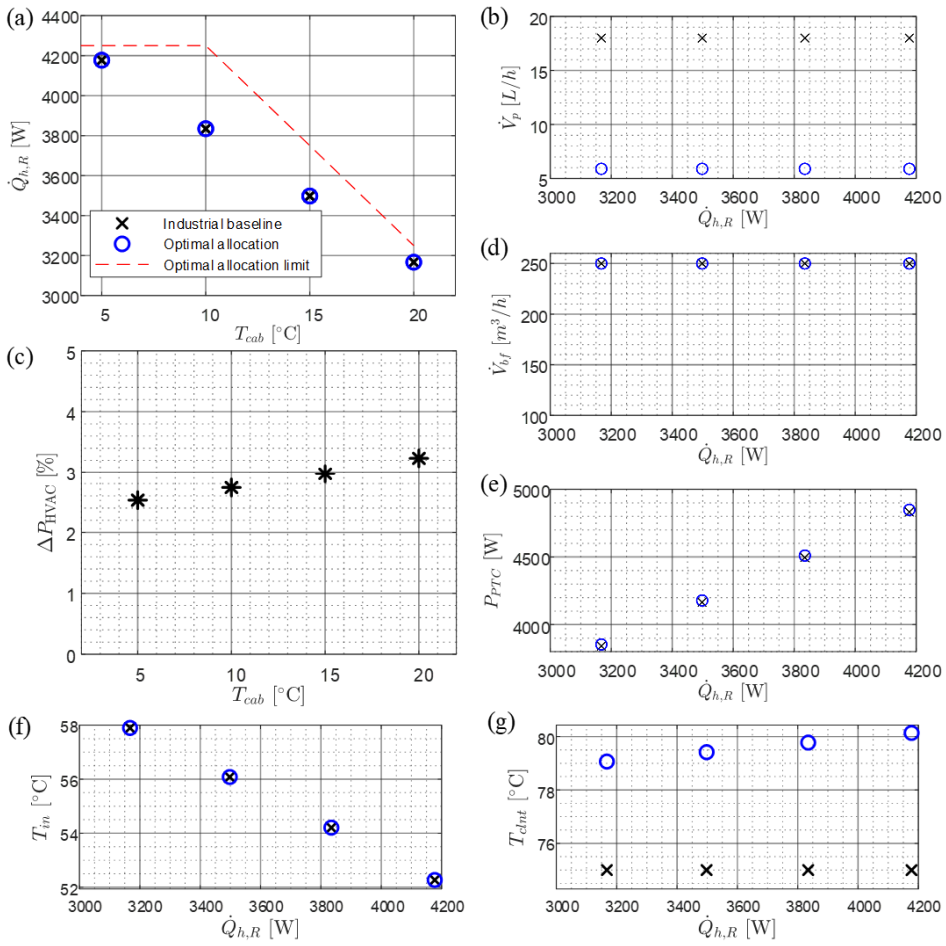



**Figure 16.** Comparative assessment of optimal allocation and industry baseline control strategies for stationary conditions.

For equal $\dot{Q}_{h,R}$ and $T_{cab}$ operating points (see Figure 16a), the control allocation (CA) strategy yields power consumption savings in the range from 2.5% to 3.2% when compared to the baseline strategy (Figure 16c). Comparison of the allocations of $\dot{V}_p$, $\dot{V}_{bf}$ and $P_{PTC}$ in Figure 16b,d,e indicates that the saving comes from significantly reduced pump flow. The air blower fan flow setpoint remains at its maximum for both strategies, while the PTC heater power is slightly higher in the CA case (to compensate for the reduced pump flow). The maximum setting of the blower fan flow is explained by the relatively small blower unit with low associated losses (Figure 2). Operating below this level would result in an increased coolant temperature at the heater core outlet, with corresponding increased energy losses through the coolant circulation system.

To gain insights in the root causes of the power savings observed in Figure 16, Table 2 compares the individual HVAC system power losses for the two control strategies and $T_{cab} = 20$ °C, where $\dot{Q}_{loss,clnt}$ denotes thermal losses in the coolant circulation system, while $P_{p,loss}$ and $P_{bf,loss}$ denote the pump and fan power losses, respectively. While the $P_{bf,loss}$ losses are expectedly equal in both cases (Table 2), a significant reduction in the pump losses $P_{p,loss}$ is observed in the case of the CA strategy, which is due to the lowered level of pump flow in that case (Figure 16b) and a progressive power loss dependency on the pump flow (Figure 2a). Conversely, the lowered pump flow leads to a coolant temperature increase (Figure 16g), resulting in higher associated coolant thermal losses $\dot{Q}_{loss,clnt}$. However, the reduction in pump losses outweighs the increase in thermal losses, resulting in reduction of the total power loss by around 20% (Table 2) and, correspondingly, a total power consumption reduction of around 3% (Figure 16c).

**Table 2.** Comparative assessment of individual HVAC system power losses for industry baseline and CA strategies at $T_{cab}$ = 20 °C.

| | $\dot{Q}_{loss,clnt}$[W] | $P_{p,loss}$[W] | $P_{bf,loss}$[W] | Σ |
|---|---|---|---|---|
| Industry baseline | 674.5 (0.0%) | 156.9 (0.0%) | 93.25 (0.0%) | 988.4 (0.0%) |
| CA | 686.8 (1.8%) | 12.4 (−92.1%) | 93.25 (0.0%) | 792.4 (−19.8%) |

In addition to the increased HVAC system energy efficiency, the CA strategy has the potential to operate at higher heating power output than the industry baseline, as illustrated by the red dashed line in Figure 16a. This implies that the CA strategy not only operates more efficiently in the (quasi-) stationary regime but can also reduce the heat-up response time (see next subsection).

### *6.2. Heat-Up Conditions*

The CA strategy has further been compared with the industry baseline for the highly transient heat-up scenario, where the high-fidelity model includes the cabin thermal model in addition to the HVAC model. Since the baseline strategy does not include the supervised cabin temperature controller, it is set to operate in the open-loop manner, with a nearly maximum heating power, set through a high feedback-controlled coolant temperature (75 °C) and high pump and blower flows (250 $m^3$/h and 18 L/min, respectively) to replicate the experimental tests described in [32]. For the sake of fair comparison, the CA strategy operates along the upper limit of heating power $\dot{Q}_{h,R}$, as shown in Figure 11, rather than being controlled by the superimposed controller.

The comparative time responses are shown in Figure 17 for two variants of the CA strategy, while the corresponding numerical results are presented in Table 3. The label CA denotes the case of the CA strategy corresponding to a nominal PTC power limit of 5 kW, and allowing for the maximum heating power limit denoted by the red dashed line in Figure 16. The label PTC Boost denotes the scenario that exploits the short-term ability

of the PTC heater to exceed its nominal power output up to 3 kW (a feature present in the baseline strategy, see Figure 17b). To resemble the baseline strategy response characterized by a relatively early and approximately linear fall in the PTC power from the boost level to the regular operating region, the CA strategy is adjusted through a ramp-down limit of the low-level controller (see Figure 17b).

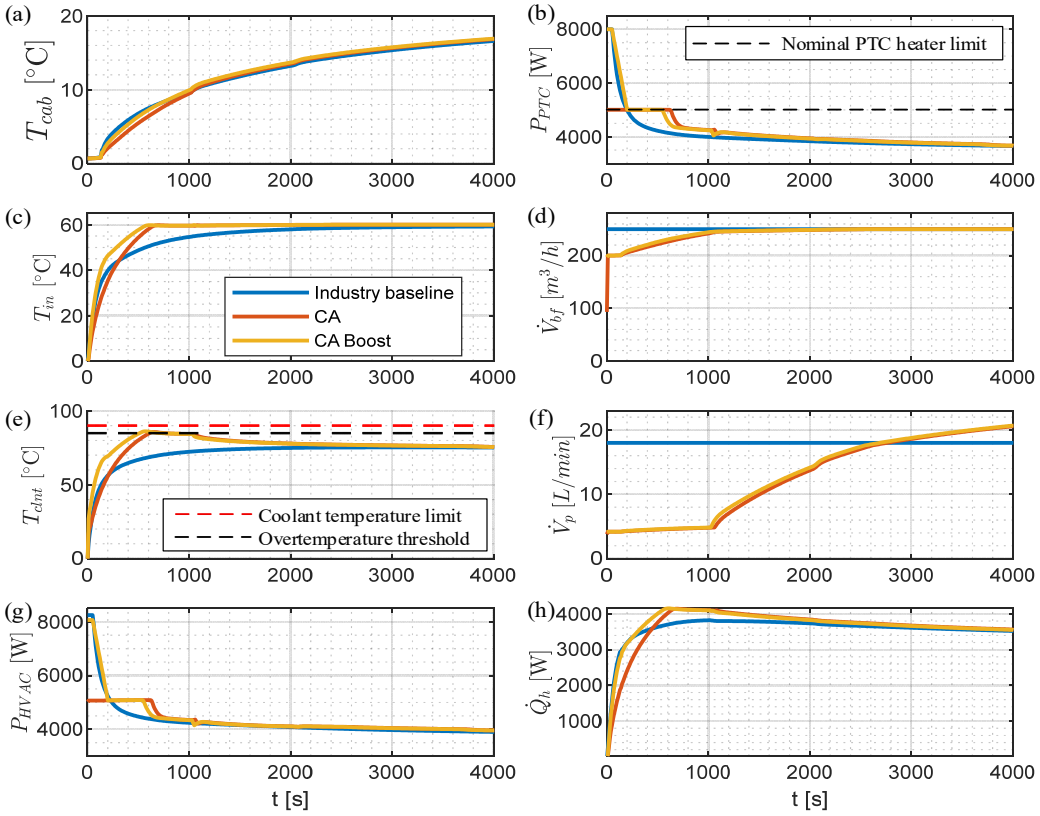



**Figure 17.** Comparative responses of control systems with two variants of control allocation strategy and industry baseline strategy for heat-up scenario.

**Table 3.** Comparison of performance indicators of two variants of control allocation strategy and industry baseline strategy for heat-up scenario.

| Control Strategy | Results at $t$ = 600 s | | | Results at $t$ = 9300 s | | |
|---|---|---|---|---|---|---|
| | $T_{cab}$ [°C] | $T_{in}$ [°C] | $E_{HVAC}$ [kWh] | $T_{cab}$ [°C] | $T_{clnt,max}$ [°C] | $E_{HVAC}$ [kWh] |
| Industry Baseline | 7.50 (0.0%) | 50.5 (0.0%) | 0.892 (0.0%) | 19.35 (0.0%) | 75.28 (0.0%) | 10.353 (0.0%) |
| CA | 6.40 (−14.6%) | 58.05 (14.9%) | 6.383 (−5.2%) | 19.47 (0.6%) | 85.75 (13.91%) | 10.526 (1.6%) |
| CA Boost | 7.26 (−3.2%) | 59.79 (18.4%) | 6.402 (6.1%) | 19.49 (0.7%) | 86.18 (14.48%) | 10.609 (1.7%) |

$E_{HVAC}$—HVAC system energy consumption, $T_{clnt,max}$—maximum achieved coolant temperature.

Table 3 presents the corresponding performance metrics for the interval of the first 600 s of the heat-up phase and the full simulation interval of 9300 s (the latter corresponds to the interval in which the measurements were originally recorded [32]). For the shorter time horizon of 600 s, the cabin temperature $T_{cab}$ rises to only around 7 °C from the initial temperature equal to the ambient temperature $T_{amb} = 0$ °C (Figure 17a). The cabin temperature values reached by the different control systems are rather comparable (Table 3, Figure 17a), indicating comparable thermal comfort for a fair comparison of the HVAC electrical energy consumption $E_{HVAC}$, as the energy efficiency metric considered. The main

differences can be observed in the cabin inlet air temperature responses (Figure 17c), where the CA strategy shows around a 15% increase in $T_{in}$ at $t$ = 600 s compared to the baseline strategy (see the $T_{in}$ column of Table 3), while the CA Boost strategy demonstrates an even bigger increase (up to around 18%). The main root cause for this improvement is exploiting a wider range of coolant temperatures (up to the declared limit of 90 °C, see Figure 17e), and consequently keeping the PTC power at higher values once the initial boost phase ceases (Figure 17b). This is paid for by a higher energy consumption $E_{HVAC}$ by a comparable margin of 6%, and is not reflected in faster cabin temperature response (in fact, the cabin temperature is lower by 3%) due to the lower CA-allocated blower fan flow (Figure 17d).

However, over the full heat-up horizon (9300 s), the energy-efficient strategy achieves an energy consumption reduction of around 2%, while the reached cabin temperature is only slightly lower (less than 1%). The observed energy saving is consistent with the stationary results from Figure 16c, with the note that the full heat-up response includes a dominant quasi-stationary (settling) temperature transient phase (see Figure 17a and note that the settling phase is even longer for the full interval of 9300 s considered in Table 3), for which the CA strategy is optimal.

## 7. Verification of Rule-Based Controller Extension

Overall, the CA strategy did not bring a considerable improvement over the baseline strategy for the heat-up scenario (see Section 6), which was the motivation for developing its extension with the DP optimization-inspired RB modification strategy tested in this section.

### *7.1. Reduced-Order Model-Based Verification*

The RB control strategy designed in Section 4 based on insights gained through DP control trajectory optimization is verified against the DP globally optimal benchmark. At the same time, the RB strategy is verified against the CA approach to assess energy efficiency gains attained through DP-inspired RB control for the heat-up scenario, for which the CA strategy is suboptimal (Section 3).

Figure 18 shows the comparative responses of state and control variables for different control approaches and the optimization/simulation duration $t_f$ = 4000 s. The RB strategy is initially delayed for 450 s to finish around the cabin temperature target of 18 °C at the end time $t_f$, for a fair comparison with the DP and CA approaches. The CA strategy starts with temporarily exploiting the PTC power boost of around 8 kW. The nearly optimal RB strategy does not need this power boost to reach the cabin temperature target, which in combination with locating the pump operating points at the knee of its power consumption map results in reduced energy consumption. Finally, Figure 18 indicates that the RB strategy with its simple rules (Section 4) manages to resemble the offline DP benchmark very well.

Table 4 presents the corresponding energy consumptions. The DP optimization results in a reduction in energy consumption by 10.6% when compared to the CA strategy, showing considerable potential for enhancement of the CA strategy for the heat-up period. At the same time, this result justifies the stationary assumption applied for CA strategy design (Section 4), with the note that the 10% performance margin is considered modest, having in mind that the stationary-designed CA law is applied to overly opposite, highly transient heat-up scenario. The RB strategy gives a comparative energy consumption reduction versus the CA approach (8.6%), thus confirming that it can approach the offline DP benchmark.

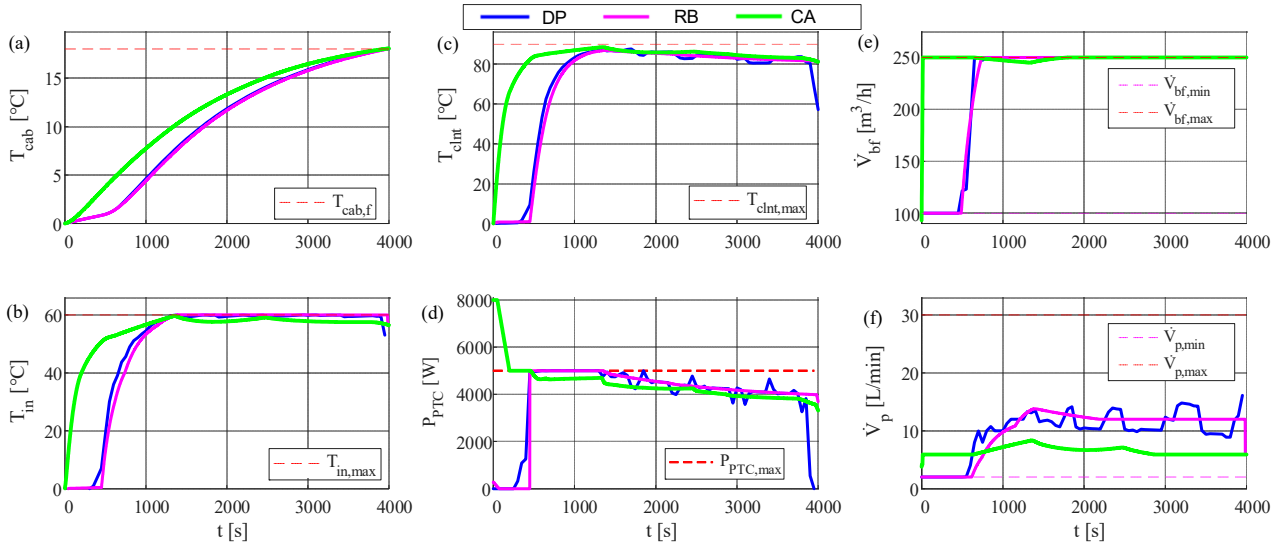



**Figure 18.** Comparative heat-up responses of HVAC system represented by reduced-order model and managed by different control approaches.

**Table 4.** Comparative energy consumption performance of HVAC systems managed by different control approaches for heat-up scenario (reduced-order model).

| | CA | DP | RB |
|---|---|---|---|
| $T_{cab}(N_t)$ [°C] | 18.07 (0.0%) | 18.01 (−0.34%) | 18.02 (−0.27%) |
| $E_{bf}$ [kWh] | 0.103 (0.0%) | 0.090 (−12.5%) | 0.091 (−12.1%) |
| $E_p$ [kWh] | 0.016 (0.0%) | 0.045 (+181%) | 0.046 (+189.4%) |
| $E_{PTC}$ [kWh] | 4.890 (0.0%) | 4.344 (−11.2%) | 4.440 (−9.2%) |
| $E_{HVAC}$ [kWh] | 5.009 (0.0%) | 4.479 (−10.6%) | 4.577 (−8.6%) |

The proposed simple-to-implement and nearly optimal RB strategy is meant to be combined with the CA strategy, where the former handles the heat-up phase and the latter provides optimal control in stationary conditions (Section 4). The combined control is illustrated in Figure 19 along with the corresponding DP-optimized trajectories. The RB-to-CA switching is set to occur when the cabin temperature reaches 18 °C, which is at $t_f = 4000$ s in this particular response. Similarly, a soft constraint is added to the DP optimization problem formulation, which requires the cabin temperature to be equal to or greater than 18 °C for $t_f \geq 4000$ s. The results in Figure 19 point out that the practical combined control strategy resembles very well the DP behavior throughout the response. A minor discrepancy observed is that the DP optimizer provides a deep drop in the control input $P_{PTC}$ immediately after the switching instant to locally reduce the losses. This behavior may be replicated by the RB-CA strategy through addition of a feedforward lead–lag compensator in the inlet temperature reference path, but with a small influence on the total energy consumption. Another discrepancy relates to certain shifts in steady-state values, which is because of differences between the high-fidelity system model (for which the CA strategy was designed) and the reduced-order model (for which the DP optimizations were conducted).

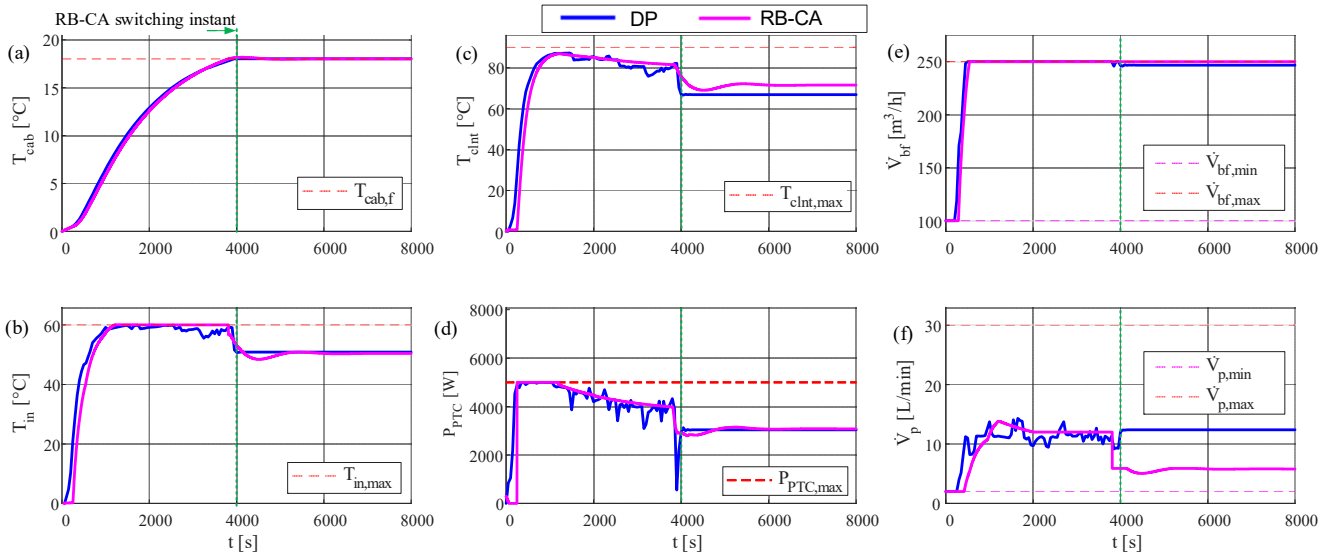



**Figure 19.** Comparative response of combined RB and CA control strategy versus the DP benchmark (note: RB activation is initially delayed to align the switching instants for two sets of responses).

### *7.2. High-Fidelity Model-Based Verification*

The RB control strategy developed in Section 4 is further verified against the CA strategy based on the high-fidelity model. The comparative heat-up simulation results are shown in Figure 20, while the corresponding quantified performance indices are given in Table 5. Evidently, the RB strategy takes around 15% less time to reach the target temperature (a shorter heat-up phase), which contributes to increased thermal comfort, while at the same time the total HVAC energy consumption ($E_{HVAC}$) is around 12% lower. In a qualitative sense these results are similar to those obtained on the simplified reduced-order model, including the fact that the RB-controlled system consumes more energy on the side of the pump and less on the side of the PTC and blower fan. Good agreement between the system behavior for the high-fidelity and simplified reduced-order models indicates a good robustness of the strategy on one hand, and a good accuracy of the reduced-order model on the other hand.

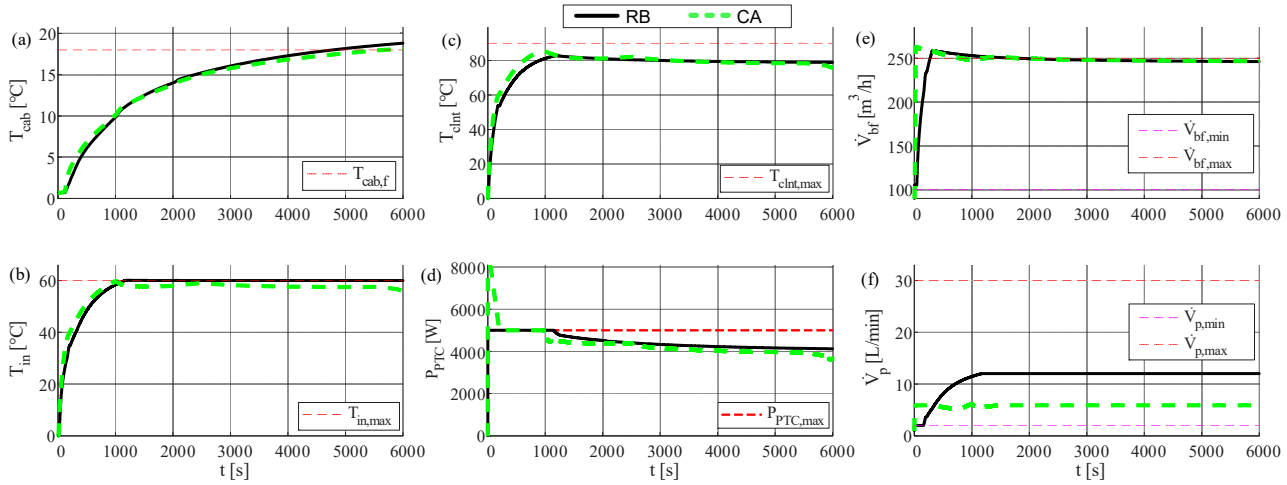



**Figure 20.** Comparative responses of RB and CA strategies obtained on high-fidelity model for heat-up scenario.

**Table 5.** Comparative performance indices corresponding to RB- and CA-controlled HVAC system operating in heat-up scenario (high-fidelity model).

| | $t_{18^\circ C}$ [s] | $E_{bf}$ [kWh] | $E_p$ [kWh] | $E_{PTC}$ [kWh] | $E_{HVAC}$ [kWh] |
|---|---|---|---|---|---|
| CA | 5680 (0.0%) | 0.1463 (0.0%) | 0.0194 (0.0%) | 6.9064 (0.0%) | 7.0720 (0.0%) |
| RB | 4785 (−15.6%) | 0.1208 (−17.4%) | 0.0570 (+193.8%) | 6.0241 (−12.8%) | 6.2018 (−12.3%) |

$t_{18\ ^\circ C}$–time elapsed until a cabin temperature of 18 °C is reached.

## 8. Conclusions

A hierarchical control allocation strategy has been proposed to effectively coordinate multiple, redundant actuators of a PTC heater-based HVAC system of an electric minibus. The control framework also integrates a superimposed passenger cabin temperature PI controller and a low-level cabin inlet air temperature PI controller, optimized for fast and well-damped responses. The former comprises reference rate and variable output limiters, while the latter is accompanied by a limiter of coolant temperature. To further enhance performance during transient operation, a dynamic-optimization-inspired rule-based (RB) strategy is integrated into the overall control framework, enabling efficient operation under both heat-up and quasi-stationary operating conditions.

The proposed control system has been validated through computer simulations under small- and high-signal operating modes using an experimentally validated vehicle model that combines high-fidelity HVAC and multi-zonal cabin submodels. Compared to an industry baseline control strategy reconstructed from vehicle data and experimental responses, the basic optimal control allocation (CA) strategy achieves battery energy savings of approximately 3% under steady-state conditions. The savings mostly arise from lower allocated coolant pump flow, which is associated with an increase in temperature and corresponding thermal losses, but in turn it reduces the pump power losses and leads to lowered total power consumption.

Performance of the basic CA strategy has further been evaluated for the transient heat-up regime. As the CA strategy is originally designed for stationary conditions, it results in only minor improvements over the industry baseline strategy for the heat-up regime. Thus, the CA strategy is enhanced through the RB extension, which enables energy consumption reductions of up to approximately 12% in the heat-up period and can be seamlessly switched back to the CA once the cabin temperature response settles, ensuring optimal stationary performance. The RB strategy initially delays activation of the blower fan and particularly the pump to promote effective coolant heat-up. The fan and pump flows are then increased gradually along with the increase in coolant temperature towards their energy-efficient setting, which, together with the maximum cabin inlet air temperature reference set, provides maximum heating power with a low energy loss.

Future work will focus on designing a more comprehensive distributed thermal comfort management strategy at the superimposed control level, including integration of localized infrared heating technology, and in-vehicle implementation and verification of the related control strategy.

**Author Contributions:** Conceptualization, L.G., B.Š., J.D. and I.C.; methodology, L.G., B.Š., J.D. and I.C.; software, L.G. and B.Š.; validation, L.G. and B.Š.; formal analysis, L.G., B.Š. and J.D.; investigation, L.G. and B.Š.; resources, J.D.; data curation, L.G.; writing—original draft preparation, L.G. and B.Š.; writing—review and editing, J.D.; visualization, L.G.; supervision, J.D.; project administration, J.D.; funding acquisition, J.D. All authors have read and agreed to the published version of the manuscript.

**Funding:** This work has been produced as part of research activity conducted through the MINDED project (Thermal and energy Management for INcreased Driving range of an Electric minibus including improved user-centric Design and thermal comfort), which has received funding from the

European Union's HORIZON EUROPE research and innovation program under grant agreement No. 101138202. The content of this publication is the sole responsibility of the MINDED consortium partners and does not necessarily represent the view of the European commission or its services.

**Data Availability Statement:** Data are available on request due to privacy restrictions.

**Conflicts of Interest:** Author Ivan Cvok was employed by the company Rimac Technology d.o.o., 10431 Kerestinec, Croatia. The remaining authors declare that the research was conducted in the absence of any commercial or financial relationships that could be construed as potential conflicts of interest.

## Abbreviations

| | |
|---|---|
| CA | Control allocation |
| DP | Dynamic programming |
| EV | Electric vehicle |
| HVAC | Heating ventilation and air conditioning |
| PI | Proportional–integral |
| RB | Rule-based |
| RH | Relative humidity |
| PTC | Positive temperature coefficient |

## Nomenclature

*Symbols*

| | |
|---|---|
| $a$ | Heat transfer parameter [W/K] |
| $b$ | Regression model parameter [-] |
| $c_p$ | Specific heat capacity at constant pressure [J/kgK] |
| $C$ | Heat capacity [J/K] |
| $G$ | Transfer function [-] |
| $J$ | Cost function [-] |
| $K$ | Penalization factor, proportional gain [-] |
| $k$ | Discrete-time step [-] |
| $P$ | Power [W] |
| $r$ | Correlation factor [-] |
| $\dot{Q}$ | Heat flow [W] |
| $q$ | Weighting coefficient [-] |
| $s$ | Laplace operator [-] |
| $T$ | Temperature [°C] |
| $t$ | Time [s] |
| $u$ | Control input [-] |
| $\dot{V}$ | Volume flow [$m^3$/s] |
| $z$ | Discrete-time Laplace operator [-] |
| $\Delta$ | Difference [-] |
| $\rho$ | Density [kg/$m^3$] |
| $\tau$ | Time constant [s] |

*Subscripts*

| | |
|---|---|
| $amb$ | Ambient |
| $bf$ | Blower fan |
| $cab$ | Cabin air |
| $clnt$ | Coolant |
| $d$ | Delay |
| $h$ | Heating |
| $hx$ | Heat exchanger |
| $in$ | Cabin inlet air |
| $p$ | Pump |

| | |
|---|---|
| $R$ | Reference |
| $rec$ | Recirculation |
| $clnt$ | Coolant |
| $th$ | Threshold |

## References


1. König, A.; Mayer, S.; Nicoletti, L.; Tumphart, S.; Lienkamp, M. The impact of HVAC on the development of autonomous and electric vehicle concepts. *Energies* **2022**, *15*, 441. [CrossRef]
2. Mądziel, M.; Campisi, T. Predicting Auxiliary Energy Demand in Electric Vehicles Using Physics-Based and Machine Learning Models. *Energies* **2025**, *18*, 6092. [CrossRef]
3. Fei, F.; Wang, D. PTC power control of electric vehicle thermal management system based on neural network feedforward. *Appl. Therm. Eng.* **2024**, *253*, 123803. [CrossRef]
4. De Nunzio, G.; Sciarretta, A.; Steiner, A.; Mladek, A. Thermal management optimization of a heat-pump-based HVAC system for cabin conditioning in electric vehicles. In Proceedings of the 2018 Thirteenth International Conference on Ecological Vehicles and Renewable Energies (EVER), Monte Carlo, Monaco, 10–12 April 2018; pp. 1–7. [CrossRef]
5. Liu, X.-A.; Zhang, F.; Zhang, Z.; Huang, Y.; Chen, L.; Li, X. A three-heat source segmented heating control strategy based on waste heat recovery technology for electric vehicles. *Energy Convers. Manag.* **2024**, *300*, 117932. [CrossRef]
6. Cvok, I.; Škugor, B.; Deur, J. Control trajectory optimisation and optimal control of an electric vehicle HVAC system for favourable efficiency and thermal comfort. *Optim. Eng.* **2021**, *22*, 83–102. [CrossRef]
7. Khayyam, H.; Kouzani, A.Z.; Hu, E.J.; Nahavandi, S. Coordinated energy management of vehicle air conditioning system. *Appl. Therm. Eng.* **2011**, *31*, 750–764. [CrossRef]
8. Rigatos, G.; Siano, P.; Cuccurullo, G.; Abbaszadeh, M. Nonlinear optimal control of heat pumps in electric vehicles. *Sci. Technol. Built Environ.* **2025**, *31*, 563–580. [CrossRef]
9. Alizadeh, M.; Dhale, S.; Emadi, A. A critical review and future prospects of control-oriented HVAC modeling strategies in electric vehicles. *IEEE Trans. Transp. Electrific.* **2024**, *10*, 7214–7235. [CrossRef]
10. He, L.; Li, P.; Zhang, Y.; Jing, H.; Gu, Z. Intelligent control of electric vehicle air conditioning system based on deep reinforcement learning. *Appl. Therm. Eng.* **2024**, *245*, 122817. [CrossRef]
11. Lajunen, A.; Yang, Y.; Emadi, A. Review of cabin thermal management for electrified passenger vehicles. *IEEE Trans. Veh. Technol.* **2020**, *69*, 6025–6040. [CrossRef]
12. Cvok, I.; Ratković, I.; Deur, J. Optimisation of control input allocation maps for electric vehicle heat pump-based cabin heating systems. *Energies* **2020**, *13*, 5131. [CrossRef]
13. Cvok, I.; Ratković, I.; Deur, J. Multi-objective optimisation-based design of an electric vehicle cabin heating control system for improved thermal comfort and driving range. *Energies* **2021**, *14*, 1203. [CrossRef]
14. Rao, A. Trajectory optimization: A survey. In *Optimization and Optimal Control in Automotive Systems*; Waschl, H., Kolmanovsky, I., Steinbuch, M., del Re, L., Eds.; Lecture Notes in Control and Information Sciences, 455; Springer: Cham, Switzerland, 2014. [CrossRef]
15. Bellman, R.E.; Dreyfus, S.E. *Applied Dynamic Programming*; Princeton University Press: Princeton, NJ, USA, 1962.
16. Yan, M.; He, H.; Sun, C.; Jia, H.; Li, M. Stochastic dynamic programming of air conditioning system under time-varying passenger condition for electric bus. *Energy Procedia* **2016**, *104*, 360–365. [CrossRef]
17. Rostiti, C.; Stockar, S.; Canova, M. *A Rule-Based Control for Fuel-Efficient Automotive Air Conditioning Systems*; SAE Technical Paper 2015-01-0366; SAE International: Warrendale, PA, USA, 2015. [CrossRef]
18. Kibalama, D.; Liu, Y.; Stockar, S.; Canova, M. Model predictive control for automotive climate control systems via value function approximation. *IEEE Control Syst. Lett.* **2022**, *6*, 1820–1825. [CrossRef]
19. Zhang, Q.; Stockar, S.; Canova, M. Energy-optimal control of an automotive air conditioning system for ancillary load reduction. *IEEE Trans. Control Syst. Technol.* **2016**, *24*, 67–80. [CrossRef]
20. Cvok, I.; Deur, J. *Control Trajectory Optimization of Electric Vehicle Heat Pump-Based Cabin Heating System*; SAE Technical Paper 2025-01-8144; SAE International: Warrendale, PA, USA, 2015. [CrossRef]
21. Schaut, S.; Sawodny, O. Thermal management for the cabin of a battery electric vehicle considering passengers' comfort. *IEEE Trans. Control Syst. Technol.* **2020**, *28*, 1476–1492. [CrossRef]
22. Cvok, I.; Deur, J. Nonlinear model predictive control of electric vehicle cabin cooling system for improved thermal comfort and efficiency. In Proceedings of the 2022 European Control Conference (ECC), London, UK, 12–15 July 2022; pp. 1759–1764. [CrossRef]
23. Grden, L.; Cvok, I.; Deur, J. Nonlinear Model Predictive Control of an Electric Vehicle Heat Pump System for Improved Energy Efficiency. In Proceedings of the 20th Conference on Sustainable Development of Energy, Water and Environment Systems (SDEWES), Dubrovnik, Croatia, 5–10 October 2025.

24. Hajidavalloo, M.R.; Chen, J.; Hu, Q.; Song, Z.; Yin, X.; Li, Z. NMPC-based integrated thermal management of battery and cabin for electric vehicles in cold weather conditions. *IEEE Trans. Intell. Veh.* **2023**, *8*, 4208–4222. [CrossRef]
25. Jia, C.; Liu, W.; Chau, K.T.; He, H.; Zhou, J.; Niu, S. Passenger-aware reinforcement learning for efficient and robust energy management of fuel cell buses. *eTransportation* **2026**, *27*, 100537. [CrossRef]
26. Widmer, F.; Ritter, A.; Achermann, M.; Büeler, F.; Bagajo, J.; Onder, C.H. Highly efficient year-round energy and comfort optimization of HVAC systems in electric city buses. *IFAC-PapersOnLine* **2023**, *56*, 10656–10663. [CrossRef]
27. Widmer, F.; van Dooren, S.; Onder, C.H. Optimization of the energy–comfort trade-off of HVAC systems in electric city buses based on a steady-state model. *Control. Eng. Pract.* **2025**, *154*, 106158. [CrossRef]
28. Zhang, N.; Lu, Y.; Ouderji, Z.H.; Yu, Z. Review of heat pump integrated energy systems for future zero-emission vehicles. *Energy* **2023**, *273*, 127101. [CrossRef]
29. Zhang, Z.; Li, W.; Shi, J.; Chen, J. A study on electric vehicle heat pump systems in cold climates. *Energies* **2016**, *9*, 881. [CrossRef]
30. Lian, Y.; Ling, H.; Zhu, J.; Lv, J.; Xie, Z. Thermal management optimization strategy of electric vehicle based on dynamic programming. *Control Eng. Pract.* **2023**, *137*, 105562. [CrossRef]
31. Ji, H.; Cai, J.; Pei, J.; He, X.; Guo, F.; Wang, Y. Research on heat pump PTC coupling heating strategy for electric vehicle. *Automot. Eng.* **2022**, *44*, 1563–1570. [CrossRef]
32. Bäuml, T.; Maric, I.; Dvorak, D.; Šimić, D.; Konrad, J. Modelling and experimental validation of the heating system and the thermal cabin model of an electric minibus. In Proceedings of the 20th Conference on Sustainable Development of Energy, Water and Environment Systems (SDEWES), Dubrovnik, Croatia, 5–10 October 2025.
33. Szikora, M.; Milcevic, M.; Acker, L.; Bäuml, T. Measurement Results of Initial Vehicle Identification; Deliverable 5.1; MINDED Project, European Commission Horizon Europe Programme. 2025. Available online: https://zenodo.org/records/15796792 (accessed on 5 March 2026).
34. Burnham, K.P.; Anderson, D.R. *Model Selection and Multimodel Inference: A Practical Information-Theoretic Approach*, 2nd ed.; Springer: New York, NY, USA, 2002.
35. Leonhard, W. *Control of Electrical Drives*, 3rd ed.; Springer: Berlin/Heidelberg, Germany, 2001.
36. Deur, J.; Pavković, D. Fundamentals of Electrical Drive Controls. *UNESCO Encycl. Life Support Syst.* **2012**, *6*, 21.
37. Isermann, R. *Digital Control Systems*; Springer: Berlin/Heidelberg, Germany, 1981.


**Disclaimer/Publisher's Note:** The statements, opinions and data contained in all publications are solely those of the individual author(s) and contributor(s) and not of MDPI and/or the editor(s). MDPI and/or the editor(s) disclaim responsibility for any injury to people or property resulting from any ideas, methods, instructions or products referred to in the content.